Correspondence and
requests for materials
should be addressed to
J.K. (kongjie@nwpu.
edu.cn)

* These authors
contributed equally to
this work.

Hierarchically porous silicon–carbon–nitrogen hybrid materials towards highly efficient and selective adsorption of organic dyes

Lala Meng*, Xiaofei Zhang*, Yusheng Tang, Kehe Su & Jie Kong

MOE Key Laboratory of Space Applied Physics and Chemistry, Shaanxi Key Laboratory of Macromolecular Science and Technology, School of Science, Northwestern Polytechnical University, Xi'an, 710072, P. R. China.

The hierarchically macro/micro-porous silicon–carbon–nitrogen (Si–C–N) hybrid material was presented with novel functionalities of totally selective and highly efficient adsorption for organic dyes. The hybrid material was conveniently generated by the pyrolysis of commercial polysilazane precursors using polydivinylbenzene microspheres as sacrificial templates. Owing to the Van der Waals force between sp²-hybridized carbon domains and triphenyl structure of dyes, and electrostatic interaction between dyes and Si-C-N matrix, it exhibits high adsorption capacity and good regeneration and recycling ability for the dyes with triphenyl structure, such as methyl blue (MB), acid fuchsin (AF), basic fuchsin and malachite green. The adsorption process is determined by both surface adsorption and intraparticle diffusion. According to the Langmuir model, the adsorption capacity is 1327.7 mg·g⁻¹ and 1084.5 mg·g⁻¹ for MB and AF, respectively, which is much higher than that of many other adsorbents. On the contrary, the hybrid materials do not adsorb the dyes with azo benzene structures, such as methyl orange, methyl red and congro red. Thus, the hierarchically porous Si–C–N hybrid material from a facile and low cost polymer-derived strategy provides a new perspective and possesses a significant potential in the treatment of wastewater with complex organic pollutants.

The pyrolysis of preceramic precursors has recently attracted considerable attention in manufacturing cera- mics with tailored compositions (Si–C,[1] Si–O–C,[2] Si–C–N,[3] or Si–B–C–N[4]) and diverse morphologies (bulk materials[5], fibers[6,7], coatings[8], tubes[9], foams[10,11], and porous components[12,13]) because of the advantages of precursor molecules designed in combination with the shaping processes. Among the polymer-derived ceramics (PDCs), the ternary silicon–carbon–nitrogen (Si–C–N) system has been intensively investigated to generate amorphous or crystalline non-oxide Si–C–N ceramics due to its exceptionally high temperature resistance[14], oxidation resistance[15], and mechanical strength[16], therefore, it can be used even in some harsh chemical condi- tions, such as high temperature, extensive wear, and corrosive media.

For PDCs, the pyrolysis temperature significantly determines the nature of the resulting structures. At a temperature above 800°C, the ceramics with dense and low porous structures can be generated[17]. When a moderate pyrolysis temperature of 400–800°C was employed, the emission of volatile species of precursor resulted in porous structures in an organic–inorganic hybrid state. High specific surface area (SSA) makes them suitable for catalytic supporters, adsorption, and removal of pollutants[18–20] For example, the foamed creamers from preceramic precursors, fillers, and blow agent by pyrolysis at a moderate temperature of 600°C can be used as an alternative material for activated carbons in hydrocarbon adsorption[18].

Moreover, when the hybrid materials are required to achieve multifunctionality, the hierarchical porosity is often desirable. For example, the macro/micro-porous structure can effectively improve the catalysis, adsorption, or separation performance of microporous materials. In general, the macropore channels provide chemical and mechanical stability, low pressure drop, and high external mass transfer rate due to the interconnected pore structures[21]. However, the micro/meso-porous structures would achieve the functionality for a given application because of large surface area. Herein, extensive research efforts have been devoted to prepare porous materials with tailored hierarchical pore structures. By using polysiloxanes and platinic acid as precursors and polystyrene beads as templates, Adam et al.[22] obtained the hierarchically ordered macro/micro Si–C–O–(Pt) foamed ceramics with high specific surface and potential in adsorption and catalyst application.
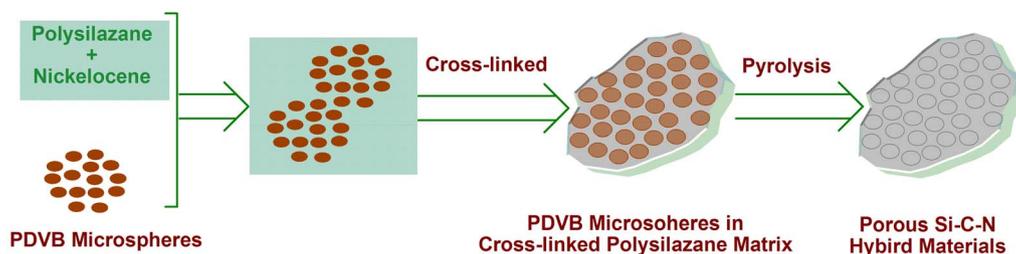
Figure 1 | Schematic illustration of preparation of hierarchically porous silicon–carbon–nitrogen hybrid materials from a pyrolysis of polysilazane and nickelocene by using polydivinylbenzene (PDVB) microspheres.

Now, various dyes effluents obtained from paper, food, plastic, textile, and cosmetic fields pose a serious threat to the environment due to their deep coloration, low biodegradability, and carcinogenicity[23,24]. Disposal of dyes from wastewater has become a significant issue. The adsorption[25], biological treatment[26], chemical coagulation[27], and photocatalytic degradation[28] have been investigated for the removal of dyes from the solution. Adsorption has shown an effective and promising perspective because of its simplicity and flexibility in design and operation[29,30]. Numerous adsorbents have been employed for removal of common dyes[31], such as metal oxide microspheres[32], carbon-based materials[33], and graphenes[34]. These methods are unfavorable in practical application because of low absorption efficiency, long absorption time, and high costs. Polymer-derived Si–C–N materials possess many distinctive advantages, such as electrochemical properties and chemical inertness. However, insignificant attention has been paid to their potential application involving removal of dyes. Notably, the Si–C–N systems possess significant potential in the field of advanced ceramics. However, the Si–C–N systems have never been employed for the separation of pollutants from wastewater. This study provides a new perspective, that by a controlled pyrolysis, it was possible to produce high SSA Si–C–N hybrid materials, which exhibited excellent adsorption performance towards dye pollutants.

In this contribution, the hierarchically macro/micro-porous Si–C–N hybrid materials were prepared by pyrolysis of polysilazane (PSZ) at a low temperature using sacrificial fillers of polydivinylbenzene microspheres (PDVB) as schematically illustrated in Figure 1. Interestingly, the porous hybrid material exhibited highly efficient and totally selective adsorption properties for triphenylmethane

dyes. Thus, the Si–C–N hybrid material, which can be mass-produced at a low cost, possesses promising potential as a novel adsorbent for the separation of organic dyes illustrated in Figure 2 (methyl blue (MB), acid fuchsin (AF), basic fuchsin (BF), methyl violet (MV), malachite green (MG), methyl orange (MO), congro red (CR) and methyl red (MR)) from aqueous solution.

Results

Pyrolysis Behavior of Polymeric Precursors. For the preparation of macro/micro-porous hybrid Si–C–N materials, the linear PSZ composed of vinyl groups and silicon hydrogen bonds (Si–H) was employed because it was one of the low-cost and general polymeric precursors for PDCs. The molecular structure of PSZ was characterized by ^{1}H NMR and gel permeation chromatography as presented in Figures S1–2 in Supporting Information. Similar to the well-known HT-1800[35], the molar ratio of silicon hydrogen bonds and vinyl groups on PSZ mainchain is 4 : 1 with a M_n of 800 g·mol^{-1}.

Figure 3 shows the pyrolysis behaviors of P1 (pure PDVB sacrificial filler), P2 (NiCp$_2$ containing polysilazane), and P3 (polysilazane with NiCp$_2$ and sacrificial filler) under nitrogen by simultaneous TGA and DSC. From the TGA curves in Figure 2a, the PDVB undergoes a dramatic thermolytic degradation in the temperature range from 430 to 500°C, in correspondence with a significant exothermic peak as presented in DSC curve (Figure 3b). The weight loss is about 80% at 1,000°C, indicating that the cross-linked PDVB microspheres retain a few residues after pyrolysis. Subsequently, for the P2 (PSZ : NiCp$_2$ = 1 : 0.04), a weight loss of 15% is observed within the temperature range from 450 to 800°C. Above 800°C, the TGA curve remains almost constant until 1,200°C. The sharp endothermic
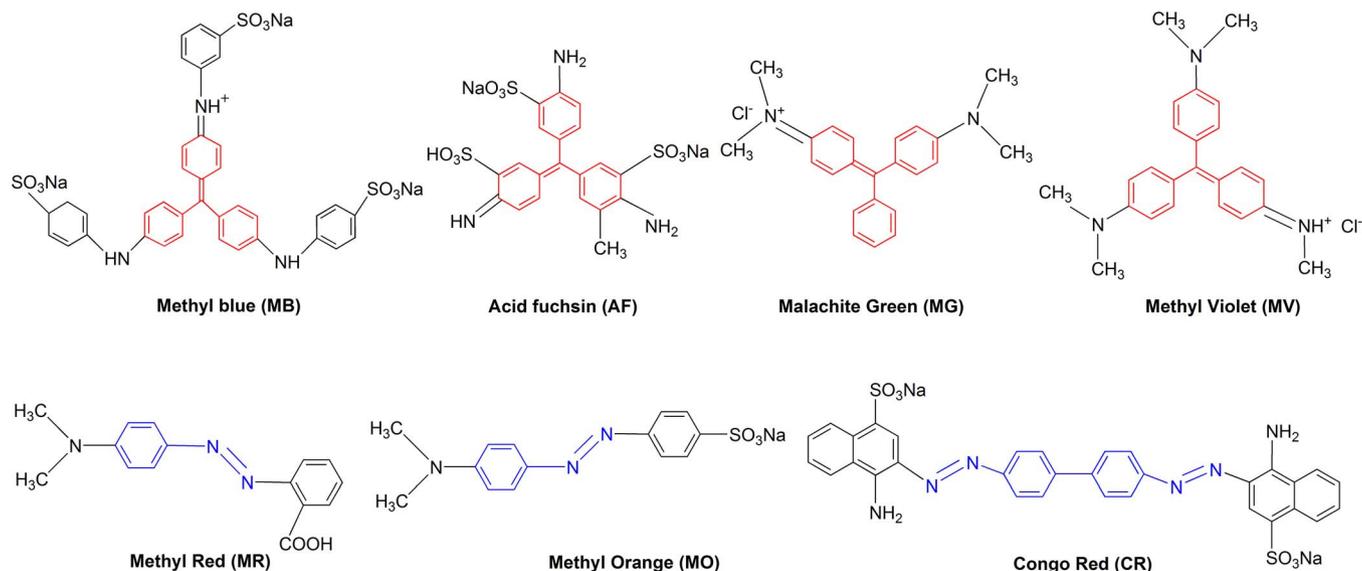

Figure 2 | The molecular structures of representative dyes, i.e. methyl blue (MB), acid fuchsin (AF), malachite green (MG), methyl violet (MV), methyl red (MR), methyl orange (MO), and congo red (CR).
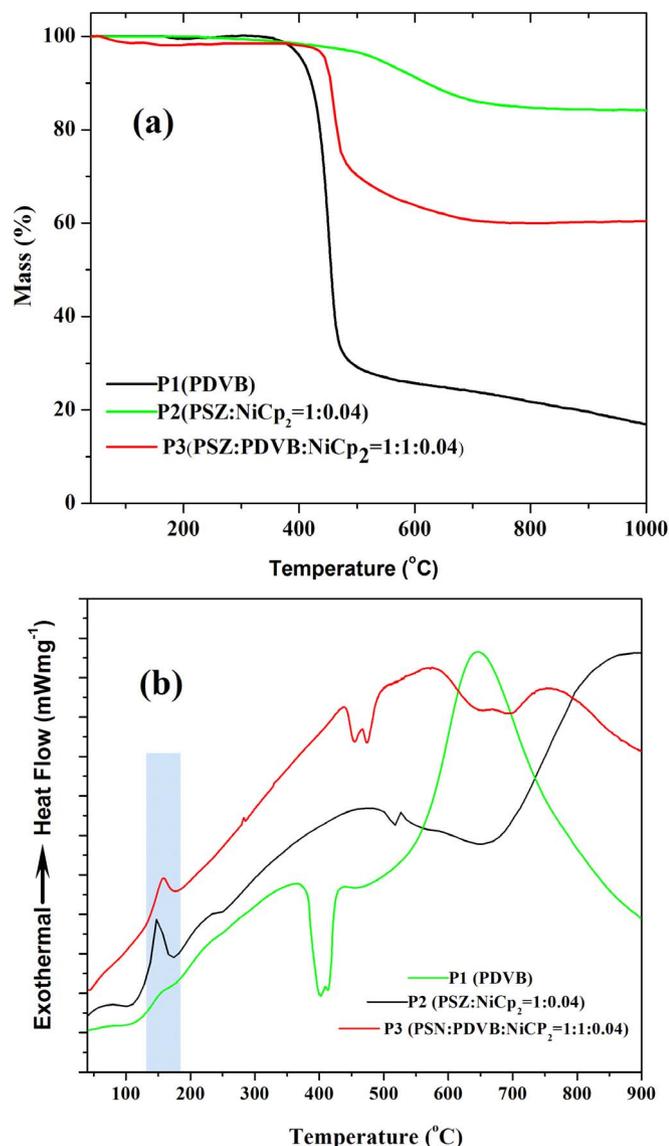
Figure 4 | The simultaneous TGA and mass spectrometry of P3 $(PSZ : PDVB : NiCp_2 = 1 : 1 : 4)$.

From the thermogram in Figure S3c for P2, the evolution of CH_4 or hydrocarbons in the temperature range of 400–900°C is ascribed to the decomposition of $Si–CH_3$ groups and cleavage of C–C bonds. The H_2 evolution is ascribed to the dehydrocoupling reaction of Si–H/Si–H or Si–H/–NH– groups. Besides, the emission of NH_3 is attributed to transamination reactions. Notably, for P2 and P3 containing $NiCp_2$, the evolution of NH_3 in correspondence with transamination reactions becomes weaker, even cannot be detected in comparison to the native PSZ in Figure S3a. Thus, the incorporation of nickel reduced the production of NH_3 from the transamination reactions and more elements are reserved, which is in agreement with the TGA curve shown in Figure 3a.

Microstructures of Hybrid Materials. The powder XRD patterns for porous hybrid materials $(PSZ : PDVB : NiCp_2 = 1 : 1 : 0.04)$ pyrolyzed at different temperature are displayed in Figure 5a. Pyrolysis at low temperature (600 and 750°C) leads to materials with complete amorphous structures. When the pyrolysis temperature is increased to 1,100°C, distinct crystalline peak is still not observed, indicating the good structural stability of porous Si–C–N materials. The broad diffraction peak at $2\theta = 26°$ indicates the presence of numerous free carbons derived from the residues of PDVB and PSZ. A main feature of PDCs is the possibility to incorporate free carbon into the matrix, which is favorable for the structural stability against crystallization and high-temperature resistance to oxidation[37]. For example, Mera et al.[38] reported that the crystallization depended on the carbon content for different precursors, and the sample with the highest carbon content was less likely to form the β-SiC phase. Herein, it could be concluded that although the incorporation of Ni was helpful for the formation of crystalline phase, the presence of carbon could render the amorphous characteristic at higher temperatures[39]. Besides, the addition of nickel could catalyze the formation of conjugated carbons (C = C, sp²) similar to polyaromatic-like conjugated structure[36,40], which might be helpful for the interaction between the porous Si–C–N material and the organic dyes.

Raman spectrum is one of powerful tools to further characterize free carbons. For the carbons with low crystallinity, Raman spectra mainly consist of a strong "sp³-like" resonant contribution and sp²-like doublet[41]. From Figure 5b, the C1 exhibits a broad peak at 1334 cm^{-1} as well as a sharp absorption peak at 1600 cm^{-1}, corresponding to carbon vibration of the so called D and G band, respectively. The D band at 1334 cm^{-1} originates from sp³-bonded carbons, and the G band at 1600 cm^{-1} is attributed to the E_{2g} vibration mode

Figure 3 | Thermograms of P1 (pure sacrificial filler), P2 ($NiCp_2$ containing polysilazane), and P3 (polysilazane containing $NiCp_2$ and sacrificial filler) obtained from simultaneous analysis by TGA/DSC under an argon atmosphere at a scanning rate of 10 K min^{-1}, (a) TGA curves, (b) DSC curves.

peak at around 170°C is related to the cross-linking reaction involving radical polymerization of vinyl groups and hydrosilylation between vinyl group and silicon hydrogen bond[36]. In terms of P3 $(PSZ : PDVB : NiCp_2 = 1 : 1 : 0.04)$, a remarkable weight loss is observed from 430 to 800°C, which is attributed to the decomposition of PDVB and chain scission of PSZ detected by simultaneous mass spectrometry.

Figure 4 shows the analysis of simultaneous TGA and mass spectrometry of P3. For the comparison, the analysis was also performed for P0 (native polysilazane), P1 (pure sacrificial filler) and P2 ($NiCp_2$ containing polysilazane) as presented in Figure S3. There exist two peaks for P3, i.e., peaks maximum at 430 and 600°C. According to the thermalgrams of P1 and P2, the first set of peaks for P3 are mainly corresponding to the decomposition products of PDVB (H_2, m/z = 2, hydrocarbons CH_x, x = 1–4, m/z = 14–16, NH_3, m/z = 17, CH_xCH_y, m/z = 25, 26, and 28) as well as other oligomer fragments (m/z = 38–74). However, another group of peaks is mainly attributed to cleavage of PSZ (H_2, m/z = 2, hydrocarbons CH_x, x = 1–4, m/z = 132–16, NH_3, m/z = 17, CH_xCH_y, m/z = 25, 26, and 28).
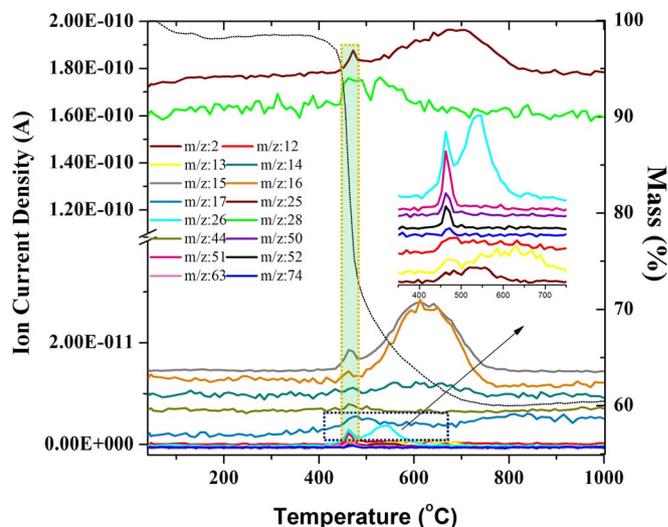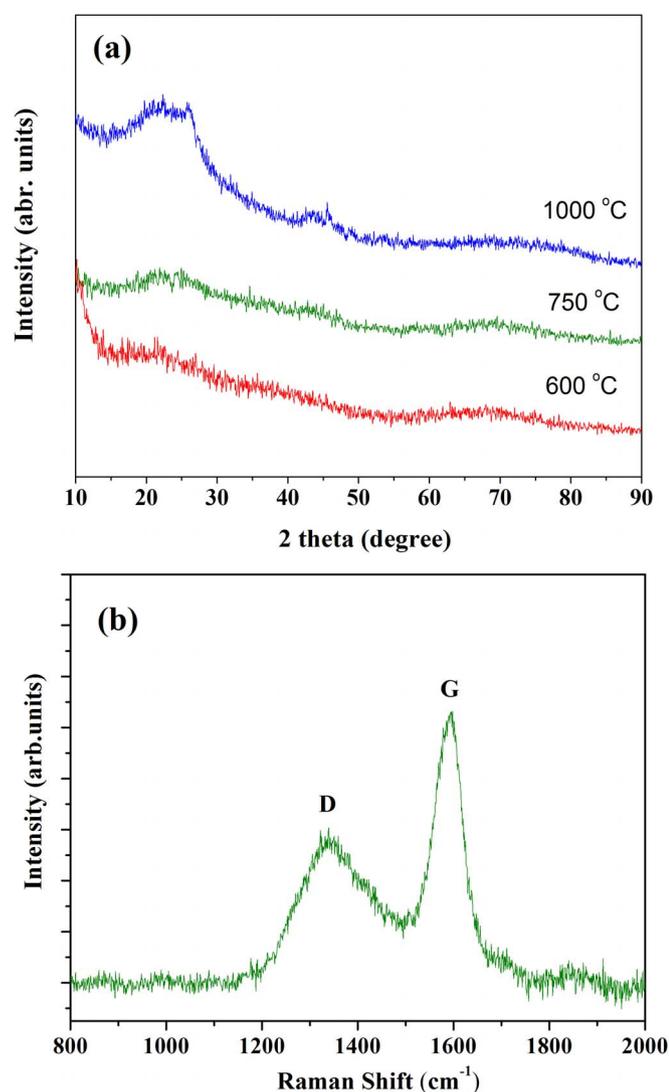
Figure 5 | (a) Powder XRD patterns of the Si–C–N porous materials obtained from P3 (PSZ : PDVB : NiCp$_2$ = 1 : 1 : 4) at 600, 750, and 1100°C, (b) Raman spectrum of Si–C–N porous materials obtained from P1 (PSZ : PDVB : NiCp$_2$ =:2 : 0.04) pyrolyzed at 600°C.

of all the sp^2 bonds of graphite[42]. Thus the Roman spectra clearly give a verification of sp^2-bonded carbons in Si-C-N hybrid materials.

Composition of Hybrid Materials. The detailed structure of porous Si–C–N hybrid material (PSZ : PDVB : NiCp$_2$ = 1 : 2 : 0.04) pyrolyzed at 600°C was evaluated by XPS as presented in Figure 6 and the according atomic composition was listed in Table 1. Obviously, the material is mainly composed of silicon, carbon, nitrogen, and nickel elements, although the peak corresponding to Ni2p is not observed because of its lower content. The Si2p peak is deconvoluted into the C–Si–O, N–Si–N, N–Si–O, and Si–O$_x$ peaks[43,44]. The C1s peak is decomposed into the C–Si, C = C, C–C, C–O–H, and C = O peaks[45–47], and the N1s peak is deconvoluted into the Si–N–C, Si–N$_x$, and Si–N–O peaks[48]. The excess content of oxygen in the 5–10 nm surface of porous material measured by XPS is mainly due to the O$_2$ absorption by powder sample before measurement. Simultaneously, a little oxygen might be obtained from the polysilazane precursors employed in the preparation.

Hierarchical Pores of Hybrid Materials. For the preparation of porous material by sacrifice filler template, the porous structure is in correspondence with the template size. Furthermore, the content

of template material also has a considerable influence on the subsequent structures in terms of interconnectivity, porosity, and wall thickness. The pyrolyzed porous structures were obtained by PSZ precursors with varied percentage of PDVB. The pyrolysis temperature was maintained at 750°C. The SEM images in Figure 7 exhibit that the porous materials possess an expected regular morphology comprised of pores. It can be clearly seen that the isolated pores are distributed uniformly in matrix when the content of filler template is relatively low. When the content of microsphere fillers is increased, the distance between the isolated pores becomes smaller and the non-contact microspheres tend to come in contact with each other to form a highly porous component. Furthermore, when the content of microsphere fillers is increased to 200%, the interconnected cellular chunks are produced and the volume of voids in the matrix increases continuously.

When the content of PDVB was relatively low, the PSZ tended to form the continuous phase and the microspheres were separately dispersed in the matrix to form the morphology similar to sea–island structure, where the size of pores in matrix was mainly 1 μm similar to the sacrificial filler. However, with increased amount of PDVB, more and more PDVB microspheres acquired access to make a contact with each other to form a sea–sea structure. In this case, the voids between microspheres were filled by PSZ, and pyrolysis fragments of PSZ were dispersed uniformly to constitute the interconnected cellular structure. Therefore, the mass transfer resistance caused by micropores during the diffusion process could be significantly reduced by the presence of interconnected macropores.

It is well-known that the maximum pyrolysis temperature plays a critical role in determining the nature of the resultant PDCs, in particular, the SSA and pore size distribution[49]. In order to investigate the influence of pyrolysis temperature on microstructure of the materials, two types of samples under different pyrolysis condition were prepared to determine the specific surface area by N$_2$ absorption–desorption measurement, i.e. C1 (PSZ : PDVB : NiCp$_2$ = 1 : 2 : 0.04, 600°C) and C2 (PSZ : PDVB : NiCp$_2$ = 1 : 2 : 0.04, 750°C). As shown in Figure 8a, the adsorption–desorption curve of C1 demonstrates a steep increase at very low relative pressures, which is a typical characteristic of microporous material with type I isotherm. Subsequently, a slow increase in the adsorption amount occurs during the relative pressure range of 0.4–0.8, indicating the presence of a few mesopores. Thus, the adsorption can be considered as multilayer adsorption and capillary condensation in these mesopores by nitrogen molecules when P/P$_0$ is below and above 0.4, respectively. The calculated BET surface area and pore volume for C1 are 251.6 m$^2 \cdot$g^{-1} and 0.09 cm$^3 \cdot$g^{-1}, respectively.

On the contrary, for C2 pyrolyzed at 750°C, the nitrogen adsorption–desorption isotherm changes from type I to type II isotherm. As shown in Figure 8b, almost no adsorption occurs at the low pressure range, indicating the disappearance of numerous micropores. With the increased P/P$_0$, the amount of nitrogen adsorbed increases very slowly. Moreover, the adsorption–desorption curves coincide well and almost no hysteresis loop can be observed, implying the absence of mesopores. The calculated BET surface area for C2 reduces drastically to 3.2 m$^2 \cdot$g^{-1} in comparison to C1. Moreover, for both C1 and C2, the adsorption capacity still increases when the relative pressure is above 0.8, indicating the presence of large pores produced by pyrolysis of PDVB. According to the literature[50], the polymer to ceramic transformation, in general, occurs in the temperature range of 500–800°C accompanied by shrinkage and density increase. The TGA and mass spectrometry curve of precursor (PSZ : NiCp$_2$ = 1 : 0.04) shown in Figure 4 displays that the ion current density reaches maximum at about 600°C confirmed by the decomposed organic moieties of the preceramic polymer (mainly CH$_x$ and CH$_x$CH$_y$), which contributes to numerous micropores in the matrix. However, the build-up of porosity is transient because it can be eliminated at an elevated temperature to achieve the ceramization
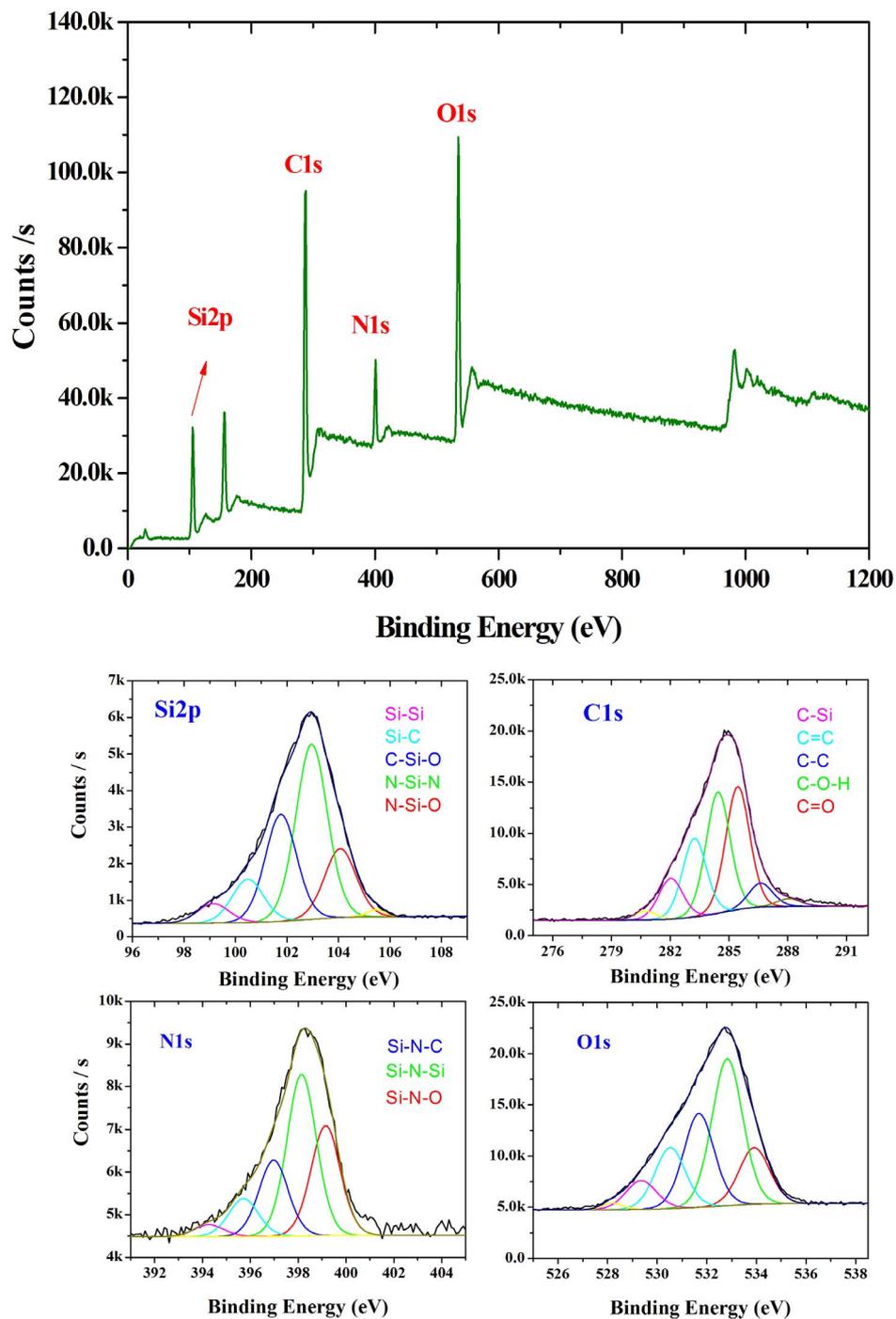
Figure 6 | XPS spectra of porous Si–C–N hybrid material from precursor (PSZ : PDVB : NiCp$_2$ = 1 : 2 : 0.04) pyrolyzed at 600°C (C1).

Table 1 | The binding energy of different bonds of Si–C–N porous material pyrolyzed at 600°C (C1)

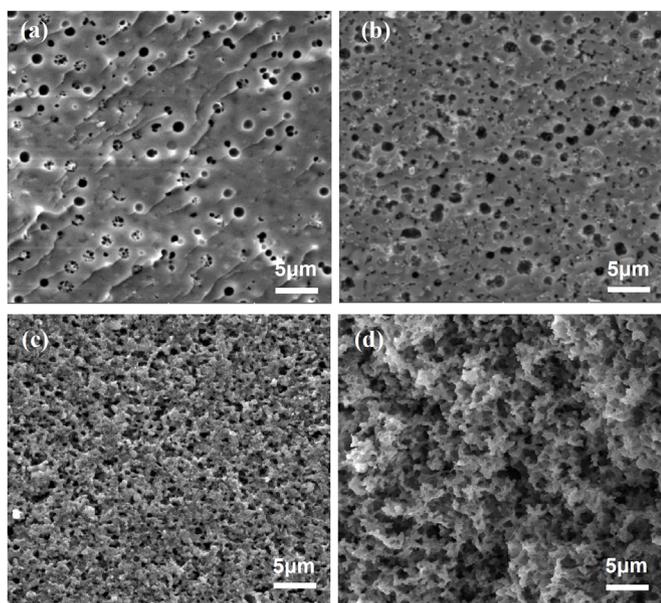| Si2p[43–44]		C1s[45–47]		N1s[48]	
Bond	Binding energy (eV)	Bond	Binding energy (eV)	Bond	Binding energy (eV)
Si-Si	99.1	C-Si	281.8-283.2	Si-N–C	396.9
Si-C	100.5	C = C	284.5	Si-N–Si	398.0
C–Si–O	101.8	C-C	285.5	Si-N–O	399.2
N–Si–N	102.9	C–O–H	286.6	—	—
N–Si–O	104.1	C = O	288.1	—	—

Figure 7 | SEM images of Si–C–N porous materials from precursors with a PSZ:PDVB:NiCp$_2$ of (a) 1:0.3:0.04, (b) 1:0.5:0.04, (c) 1:1:0.04, (d) 1:2:0.04.

process[51]. The BET results in combination with those from SEM analyses clearly indicate the presence of hierarchical macro/micropore structures in Si–C–N material at a low pyrolysis temperature of 600°C. Herein, the C1 with high BET surface area was selected as the target material to investigate the adsorption performance for organic dyes.

Adsorption Kinetics. From the viewpoint of adsorption kinetics, the adsorption is a heterogeneous process that involves physical, chemical, and electrostatic interactions. The adsorption rate of dyes depends on the contact time of the solid and liquid as well as on diffusion process. The temporal evolution of UV spectra for two dyes of MB and AF on C1 dyes is presented in Figure 9, and the adsorption kinetic curves are presented in Figure 10. The C1 exhibits an excellent adsorption performance for two dyes. In general, the removal efficiency of 83.5% and 70.1% can be achieved within the first 60 min for MB and AF, respectively, with the initial concentration of 200 mg·L^{-1}. The adsorption removal of two dyes was rapid at the initial period (10 min) and then became slow with the increased contact time until equilibrium. The removal rate of pollutants is initially rapid, however, it gradually decreases with increased time until it reaches equilibrium. This phenomenon is ascribed to the fact that a large number of vacant adsorption sites on C1 are available at the initial adsorption stage, and after a lapse of time, the remaining vacant sites are difficult to occupy because of repulsive forces between the dye solute molecules on the solid and bulk phases[52].

To study the transient adsorption behavior of dyes, two common chemical reaction kinetic models, i.e., pseudo-first-order (PF) and pseudo-second-order (PS) kinetic models, were used to analyze the adsorption process. The linearized pseudo-first-order kinetic model is expressed as follows[53].

$$\log (Q_e - Q_t) = \log Q_e - \frac{K_1}{2.303} t \qquad (1)$$

where Q_e and Q_t are the amounts of dye adsorbed (mg·g^{-1}) at an equilibrium and time t (min), respectively. The K_1 is the rate

constant of the pseudo-first-order kinetic model (1/min). The linear form of pseudo-second-order kinetic model is given by the following equation.

$$\frac{t}{Q_t} = \frac{1}{K_2 Q_e^2} + \frac{t}{Q_e} \qquad (2)$$

where K_2 (g·mg^{-1}·min^{-1}) is the rate constant for the pseudo-second-order reaction. Figure 10b shows the fitting data to the pseudo-second-order kinetic model. Accordingly, the kinetic parameters and the correlation coefficients R^2 are determined by nonlinear regression and are listed in Table 2. The value of R^2 clearly indicate that pseudo-second-order kinetic model achieves a better fitting of the experimental data for two dyes and the calculated Q_e values ($Q_{e,cal}$) are close to the experimental values ($Q_{e,exp}$). Therefore, the pseudo-first-second kinetic model is more appropriate to characterize the adsorption behaviors of two dyes onto C1 compared to the pseudo-first-order model (see Figure S4) and the adsorption rate depends on the amount of solute at equilibrium[54].

To obtain a deep understanding on the characteristics of the adsorption process, the pore-diffusion (intraparticle diffusion) model presented by Webber was also applied to fit the experimental data[55]. The intraparticle diffusion model can be expressed by the following equation.

$$Q_t = K_t t^{1/2} + C \qquad (3)$$

where K_t is the intraparticle diffusion rate constant (g·mg^{-1}·min$^{0.5}$) and C is a constant providing the information about the thickness of the boundary layer. In Figure 11, the plots of Q_t vs. $t^{1/2}$ show at least two linear segments in correspondence with different stages in adsorption. For two linear plots, the Q_t vs. $t^{1/2}$ have intercept value far from zero, which indicates that intraparticle diffusion is not the rate-controlling step of the adsorption process and the external mass transfer may be significant in the rate-controlling step. The first segment is attributed to the outer diffusion due to the mass transfer from the dye solution to the outer surface of the adsorbent (film diffusion or boundary layer diffusion). The second portion indicates a steady adsorption step, corresponding to the diffusion of adsorbate from the adsorbent exterior to the pores or capillaries of the adsorbent internal structure (inner diffusion)[56]. Thus, the presence of multilinearity and the boundary layer thickness indicate that the adsorption of two dyes on C1 is a complex process and both the surface adsorption and intraparticle diffusion occur during the adsorption process[57].

Adsorption Isotherm. Figure 12a shows the adsorption isotherms of the two dyes on C1 at 25°C. The results reveal that the porous material exhibits excellent adsorption ability toward two dyes. For example, the removal percentage can be as high as 99.2% and 97.2% when the initial concentrations were 300 mg L^{-1} for MB and 200 mg·L^{-1} for AF, respectively. In the low concentration range, the equilibrium adsorption capacities for all the dyes increase linearly with the increased initial concentrations. However, the linear growth of the adsorption capacities is retarded at higher initial concentrations because numerous dye molecules found difficulty in accessing vacant sites of the adsorbent, most of which have been occupied. The isotherms are all L-type, which reveals that the porous material has high affinity toward these dyes.

The Langmuir and Freundlich isotherm models were adopted to fit the isotherm data and the fitting parameters are listed in Table 3. The Langmuir model is based on the assumption that the adsorption process is a monolayer adsorption on a homogeneous adsorbent surface[58]. These binding sites are finite and have the same affinity
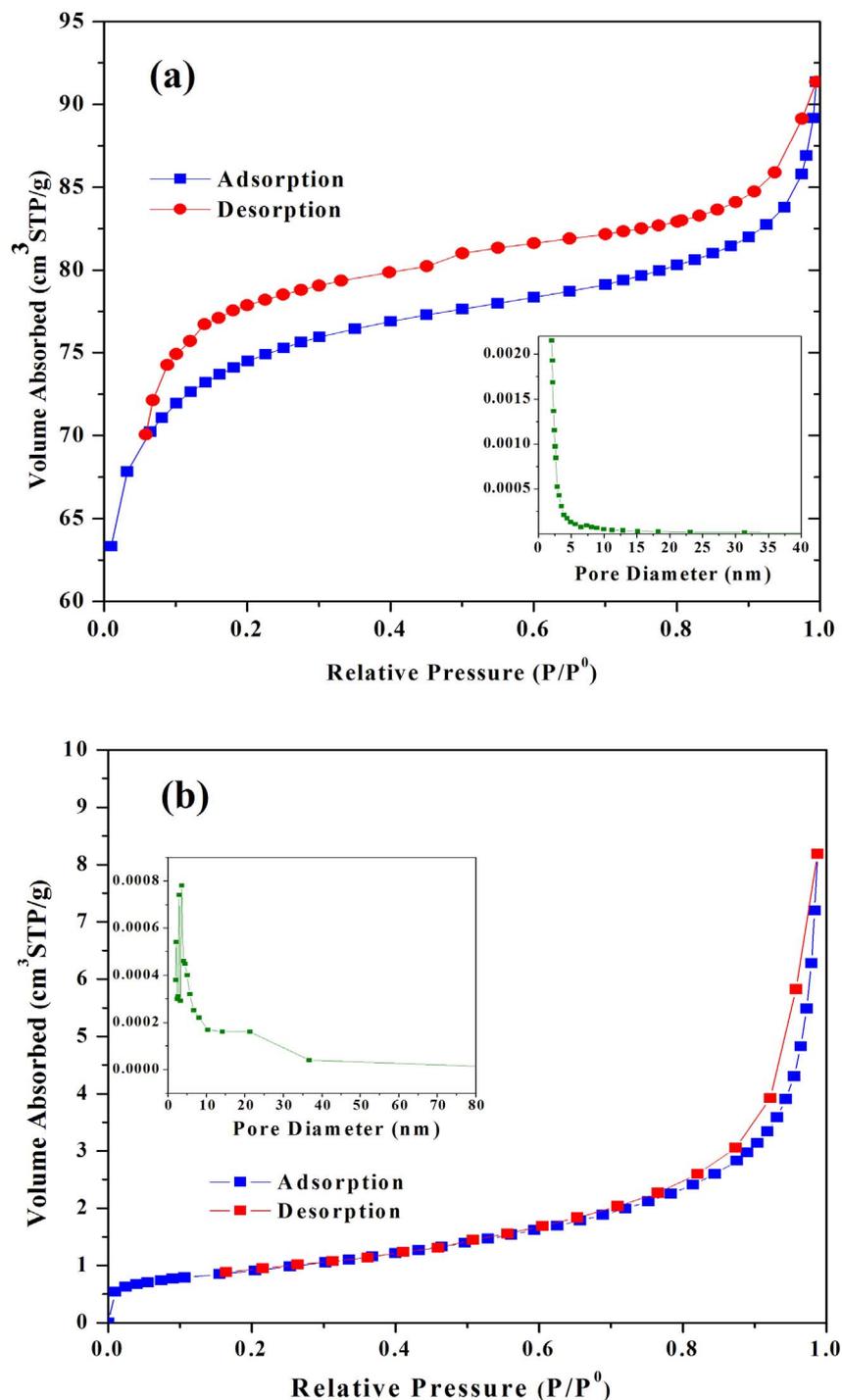
Figure 8 | Nitrogen adsorption–desorption isotherms and the corresponding pore size distribution (PSD) calculated using adsorption branch of the BJH algorithm for (a) C1 and (b) C2.

for adsorbate. Besides, there is no interaction between adsorbed molecules. The linearized Langmuir equation is expressed as follows.

$$\frac{C_e}{Q_e} = \frac{C_e}{Q_m} + \frac{1}{K_L Q_m} \tag{4}$$

where C_e (mg·L^{-1}) is the equilibrium dye concentration in liquid phase, Q_e (mg·g^{-1}) is the equilibrium adsorption capacity, Q_m (mg·g^{-1}) is maximum adsorption capacity, and K_L (L·mg^{-1}) is the affinity parameter. The fitting experimental data of Langmuir isotherm model

are shown in Figure 12b indicating that the fitting results give high linearity with correlation coefficient of 0.99975 for MB and 0.99984 for AF. Moreover, it suggests that the adsorption of two dyes on C1 is monolayer in nature and the surface is homogeneous. The calculated maximum adsorption capacity according to Langmuir isotherm model is 1327.7 mg·g^{-1} for MB and 1084.5 mg·g^{-1} for AF. The adsorption capacity of two dyes onto C1 is much higher than that of many other adsorbents, such as magnetic chitosan grafted with graphene oxide and organo-bentonite (compared to adsorption for MB), modified cellulose and carbon nanotube-graphene hybrid aerogel (compared to adsorption for AF). The values indicating
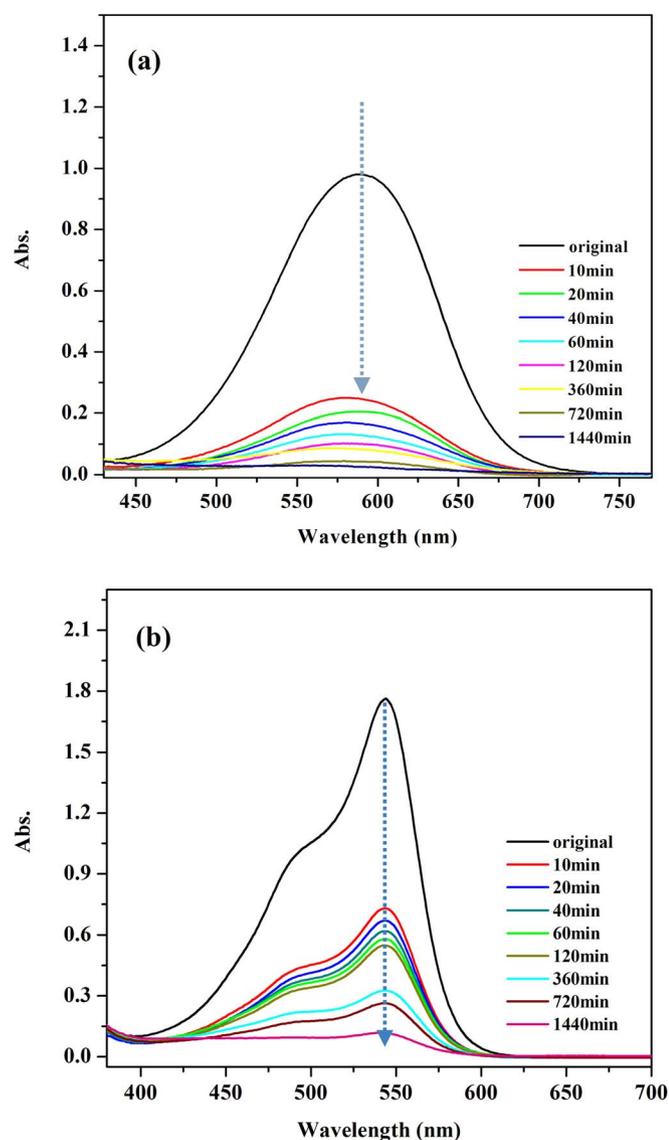
Figure 9 | The temporal evolution of UV spectral of two dye solution in the presence of Si–C–N porous material (a) MB (b) AF.

the comparison of adsorption capacities for MB and AF onto various adsorbents are listed in Table 4. Although the adsorption capacity for MB is not so high compared to barium phosphate nano-flake and β-cyclodextrin chitosan nanoparticles; the facile preparation process, good recyclability, and low cost of Si–C–N hybrid materials are more favorable in wastewater treatment[59–66].

In contrast, the Freundlich isotherm model is, in general, used to describe the adsorption on a heterogeneous surface with interaction between adsorbed molecules and is not restricted to the formation of a monolayer[67]. The linearized expression of this model is given by equation (7).

$$LnQ_e = LnK_F + (1/n)LnC_e \qquad (5)$$

where Q_e is the amount of dye adsorbed per gram of adsorbent ($mg \cdot g^{-1}$), C_e is the equilibrium dye concentration in solution ($mg \cdot L^{-1}$), K_F ((mg/g)·(L/mg)$^{-1}$) is the Freundlich constant, and $1/n$ is the heterogeneity factor. The fitting plots of Freundlich isotherm model for the absorption of dyes on C1 are shown in Figure S5. The Freundlich model fails to describe the experimental data, which indicates the presence of homogeneous adsorption sites on the porous Si–C–N hybrid material.
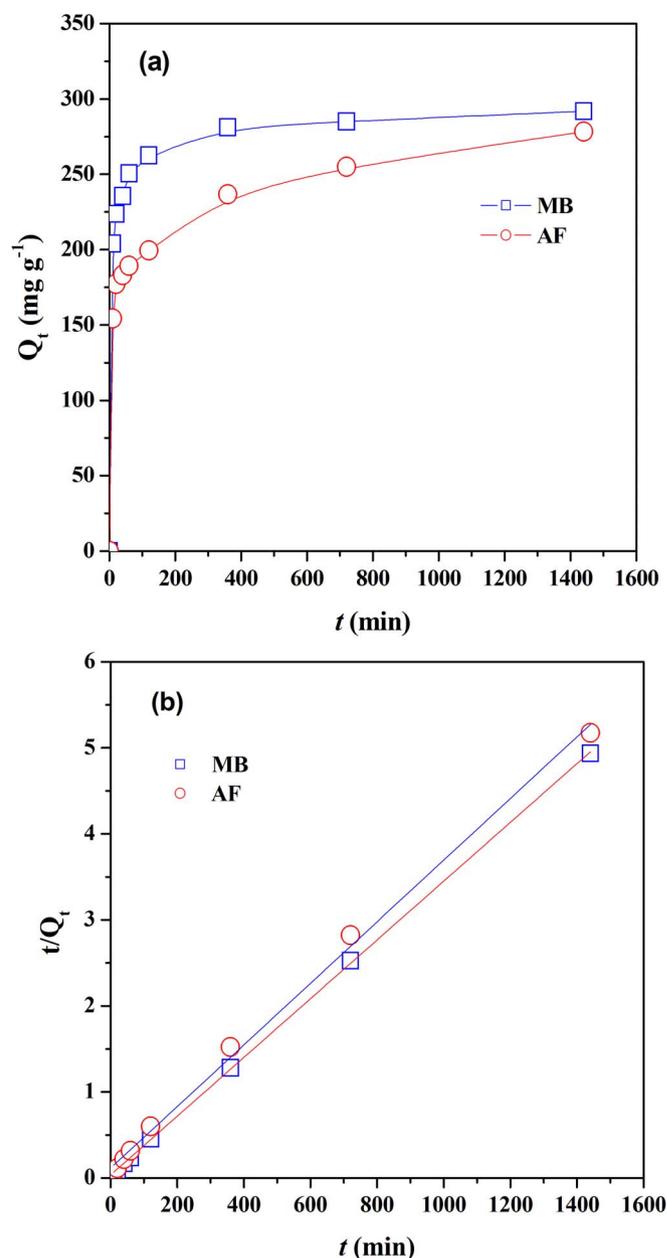
Figure 10 | (a) Adsorption kinetics curves and (b) pseudo-second-order kinetic plots for the adsorption of two dyes on C1 (initial concentration: 200 mg L^{-1} for MB and AF, dosage of C1: 666 mg L^{-1}).

Besides, the thermodynamic parameters were calculated to predict the process of adsorption by free energy of adsorption (ΔG^0), which is expressed as follows[68].

$$\Delta G^0 = -RTLnK_0 \qquad (6)$$

where K_0 is the equilibrium constant at a certain temperature, and R is the gas constant. For an adsorption reaction, K_0 is defined as follows.

$$K_0 = \frac{a_s}{a_e} = \frac{v_s}{v_e} \cdot \frac{Q_e}{C_e} \qquad (7)$$

where a_s is the activity of adsorbed dye, a_e is the activity of dye in solution at equilibrium, Q_e is the amount of dye adsorbed by per unit mass of adsorbent ($mg \cdot g^{-1}$), v_s is the activity coefficient of the

Table 2 | The fitting results of the pseudo-first-order and pseudo-second-order kinetic models to the experimental data

dye	$Q_{e,exp}$(mg g^{-1})	2nd-order kinetic model $t/Q_t = 1/(K_2Q_e^2) + t/Q_e$			1st-order kinetic model $\log(Q_e - Q_t) = \log(Q_e) - (k_1/2.303)t$		
		$Q_{e,cal}$(mg g^{-1})	$K_2(\cdot 10^4)$ (g mg^{-1} min^{-1})	R^2	$Q_{e,cal}$(mg g^{-1})	$K_1(\cdot 10^3)$ (g mg^{-1})	R^2
MB	291.8391	292.3976	3.304	0.99987	80.978	4.030	0.68619
AF	278.8342	279.33	1.121	0.99705	131.659	2.372	0.72439

^{a}Initial concentration: 200 mg L^{-1} for MB and FA, dosage of porous adsorbent: 666 mg L^{-1}.

adsorbed dye, and ν_e is the activity coefficient of dye in solution. The concentration of dye in the solution decreases and reaches zero; therefore, K_0 can be obtained by plotting $L_n(Q_e/C_e)$ *vs.* Q_e and extrapolating Q_e to zero, as shown in Figure 13. The value of R^2 obtained from a linear regression analysis is 0.90267 and 0.86085 for MB and AF, respectively. The value of K_0 from the straight line intercept with the vertical axis is 6.09 for MB and 5.32 for AF. Accordingly, the ΔG^0 values are -4.48 kJ·mol^{-1} for MB and -4.14 kJ·mol^{-1} for AF. It confirms that the adsorption of dyes onto C1 is spontaneous and thermodynamically favorable.

Selective adsorption, regeneration and recycling properties. The selective adsorption experiments were performed on several other dyes with different molecular structures as presented in Figure 14 and Figure 15. The results exhibit that the porous Si–C–N hybrid material also shows totally selective adsorption property, i.e. high adsorption capacity for MG, MV and BF and no adsorption for MO, MR and CR. It seems to be that all dyes with bulky triphenyl structure can be absorbed by C1, however, the dyes with azo benzene (MO, MR, CR) cannot be absorbed. The repeatability is also important for an adsorbent for its feasible and practical application. The hybrid material could be easily regenerated by sintering because of its resistance to high temperature. In this study, MB was used as the model dye to investigate the recyclability of porous Si–C–N hybrid material. Figure 16 shows the removal percentages of MB in five recycle runs using regenerated C1. It was observed that the removal efficiency was 96.94 and 96.11% in the first two runs and decreased slightly to 94.33% and 93.56% in the fourth and fifth runs, respectively. The good repeatability was attributed to the stability of sp^2 hybridized carbons as well as good structural stability of amorphous Si-C-N

framework at the temperature below 600°C, which ensured enough adsorption sites for five recycling process to treat the low concentration dye solution (C_0 = 200 mg·L^{-1}). Moreover, Figure S6 shows the XPS analysis performed on the sample C1 recycled after five runs (C1-five). Compared to the original C1, the surface elemental composition of C1-five underwent some modifications.
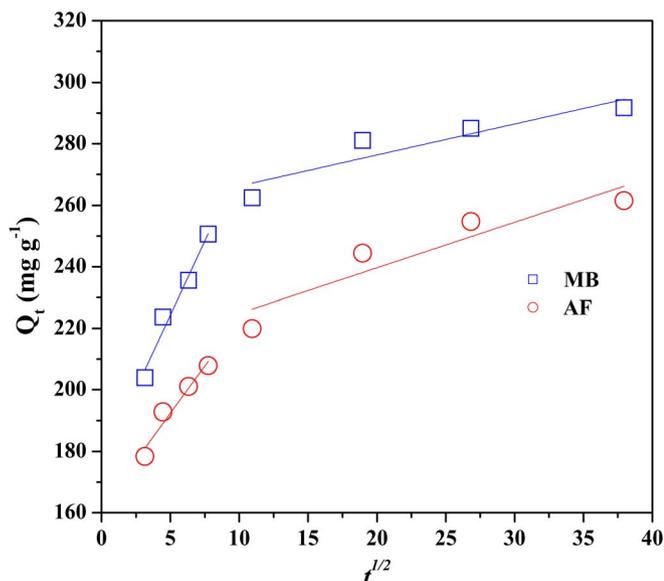

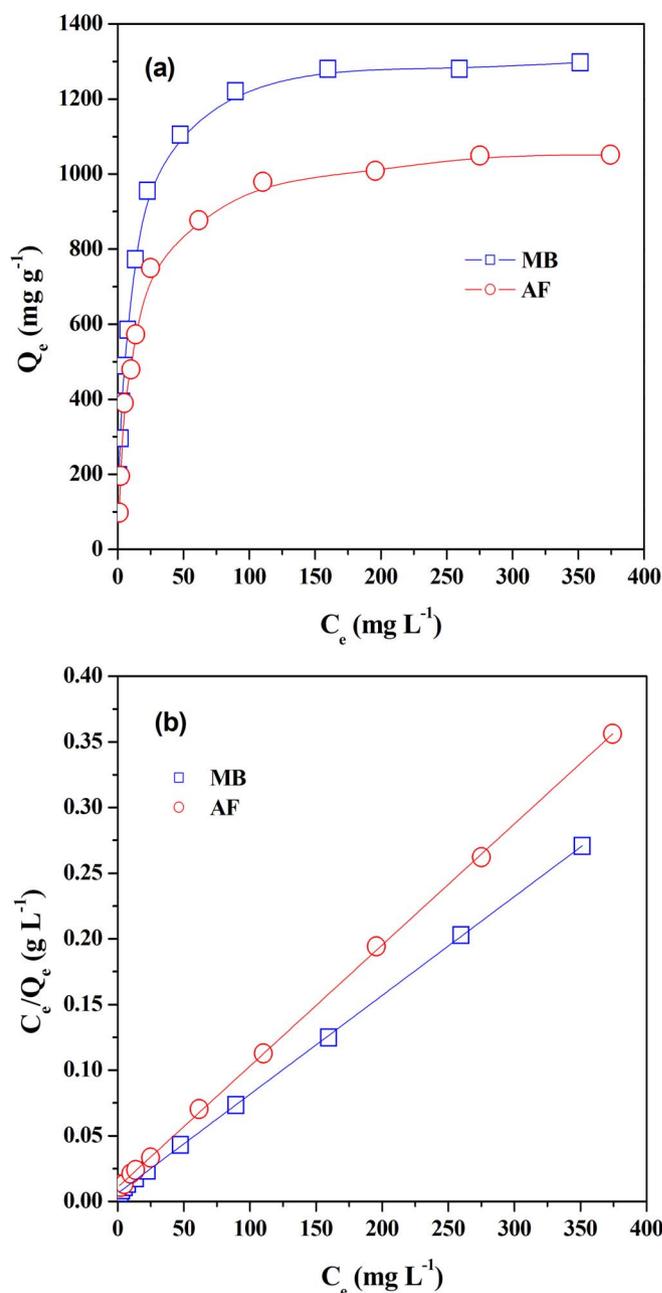**Figure 11 | Pore-diffusion model plots for the adsorption of MB and AF on C1.**

Figure 12 | (a) Adsorption isotherms of two dyes on C1 and (b) Fitting plots of Langmuir isotherm models for two dyes on C1.

Table 3 | Summary of the Langmuir and Freundlich isotherm model parameters for the adsorption of two dyes on porous Si–C–N hybrid material

isotherm	parameter	dye	
		MB	AF
Langmuir	Q_m(mg g^{-1})	1327.69	1084.45
	K_L(L mg^{-1})	0.12089	0.08475
	R^2	0.99984	0.99975
Freundlich	parameter	272	173
	n	3.20	2.92
	R^2	0.89304	0.82843

The results of the calculations revealed that the relative content of silicon and nitrogen decreased, however the relative content of carbon and oxygen increased dramatically compared to the composition of C1. However, the adsorption efficiency did not change significantly, indicating the good adsorption properties. Therefore, it was expected that this material was promising in the practical application of adsorption of dyes from wastewater.

Discussion

First, we conclude that the porous Si–C–N hybrid material selectively adsorb the dyes with triphenyl structure because of the Van der Waals force between the sp^2-hybridized carbon domain in adsorbent (proved by Raman spectrum and FTIR) and the triphenyl structure of dyes. Herein, the semiemperical quantumchemical method AM1 (Austin Model #1) was adopted to determine Van der Waals forces between sp^2-hybridized carbon domains in Si–C–N hybrid material and dyes although it seems rough for the quantitative canculation[69]. According to the results of AM1 modeling in Figure 17 and Figure S7, the atomic distance between sp^2 carbon clusters of porous Si–C–N hybrid material and MB is between 3.84 to 4.49Å, which is within the typical range of Van der Waals distance (3–4Å). However for MO, the atomic distance between carbon clusters and AF is between 5.50–5.87Å, which is beyond the typical range of Van der Waals distance. So, it is believed that the adsorption sites on porous Si–C–N hybrid material may be related to the presence of sp^{2}carbons that are proved by Raman spectra in Figure 5b. Thus, the Van der Waals forces between carbon atoms (sp^2) in porous hybrid material and the triphenyl structure of dyes may be the main driving force for the adsorption of MB, AF, MG, MV, or BF. On the other hand, the electrostatic interaction between the Si-NH-Si sites in porous Si–C–N hybrid material and amino groups in dyes should also be considered. The presence of -NH, -NH$_2$, N$^+$ in MB, NH and NH$_2$ in AF, MG and MV, is beneficial to the electrostatic interaction to Si–C–N hybrid material. While the presence of electron-donating groups, such as -N = N- in MO, MR, CR, is hindered to the electrostatic interaction to Si–C–N hybrid material as illustrated in Figure 17.
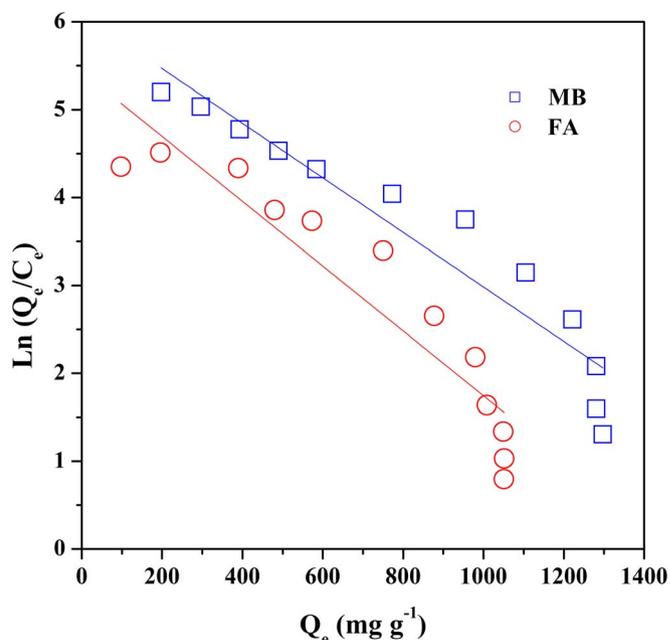

Figure 13 | Plots of Ln(Q_e/C_e) vs. Q_e for the calculation of thermodynamic parameters.

The FTIR spectroscopy and XPS analyses were performed to gain insights into the adsorption mechanism. The analyses of FTIR spectra of C1, MB/AF, and MB/AF adsorbed C1 (MB-C1/AF-C1) are presented in Figure S8. For C1, the symmetric deformation vibration corresponding to Si–CH$_3$ at 1268 cm^{-1} is still present. Similarly, the peak at 2924 cm^{-1} related to the C–H asymmetric stretching vibrations (C (sp^3) –H band) is faintly visible, indicating the presence of saturated groups. An intense and broad peak at 3440 cm^{-1} indicates the retention of N–H bond which is consistent with the mass spectrometry analysis. Importantly, the broad peaks at 1624 and 1404 cm^{-1} are ascribed to the conjugated bands of free carbons (C = C, sp^2), which is indicative of a polyaromatic-like conjugation structure. Besides, the intense peak at 1032 cm^{-1} is attributed to amorphous Si–NH–Si phase, which is also important for the adsorption of dyes. After absorption of MB on C1 (C1-MB), the characteristic peaks of MB, such as the ring stretch at 1577 cm^{-1} and three peaks at 1122, 1037, and 616 cm^{-1} corresponding to sulfonate groups, are recorded in the spectrum of the adsorptive adduct, indicating that MB has been anchored to the surface of C1. In the case of AF adsorbed C1 (C1-AF), the characteristic peaks of AF, such as the peaks at 1625 and 1584 cm^{-1}, respectively, related to NH$_2$ and aromatic rings of AF and the two peaks at 1037 and 629 cm^{-1} derived from sulfonate groups of AF, are recorded in the spectrum of the adsorptive adduct, which indicates that AF has been attached to the

Table 4 | The comparison of the maximum adsorption capacity of MB and AF on porous Si–C–N hybrid material with other adsorbents

| dye	adsorbents	adsorption capacity (mg g^{-1})	ref.
MB	magnetic chitosan grafted with graphene oxide	95.3	53
	Mn/MCM-41	131.6	54
	organo-bentonite	98.2	55
	barium phosphate nano-flake	1500	56
	magnetic-cyclodextrin chitosan	2780	57
	porous Si–C–N hybrid material	1327.7	this study
AF	modified cellulose	105.7	58
	fixed-bed column	181.82	59
	carbon nanotube–graphene hybrid aerogels	66.4	60
	porous Si–C–N hybrid material	1084.5	this work
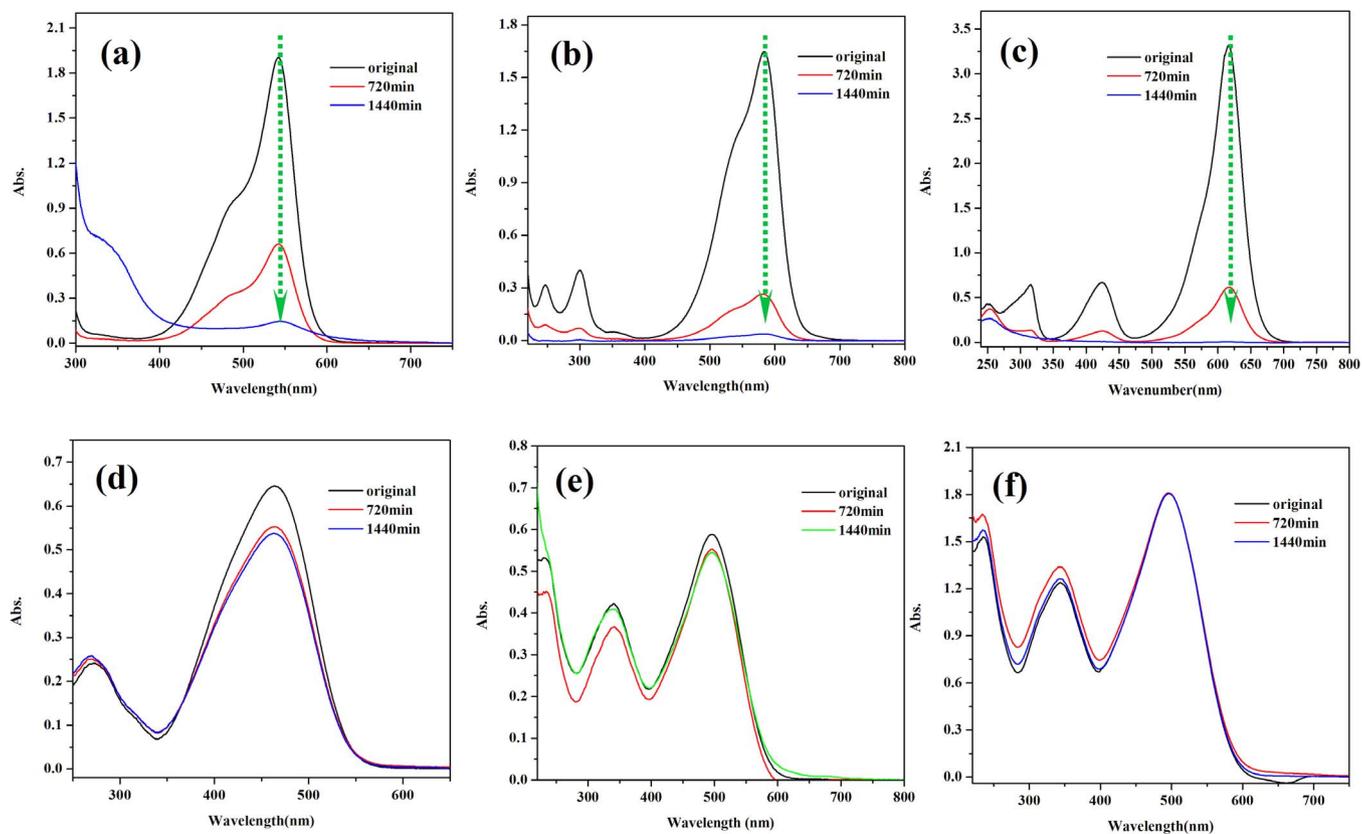
Figure 14 | Adsorption behaviors of C1 for different dyes (a) basic fuchsin, (b) methyl violet, (c) malachite green, (d) methyl orange, (e) congo red, and (f) methyl red.
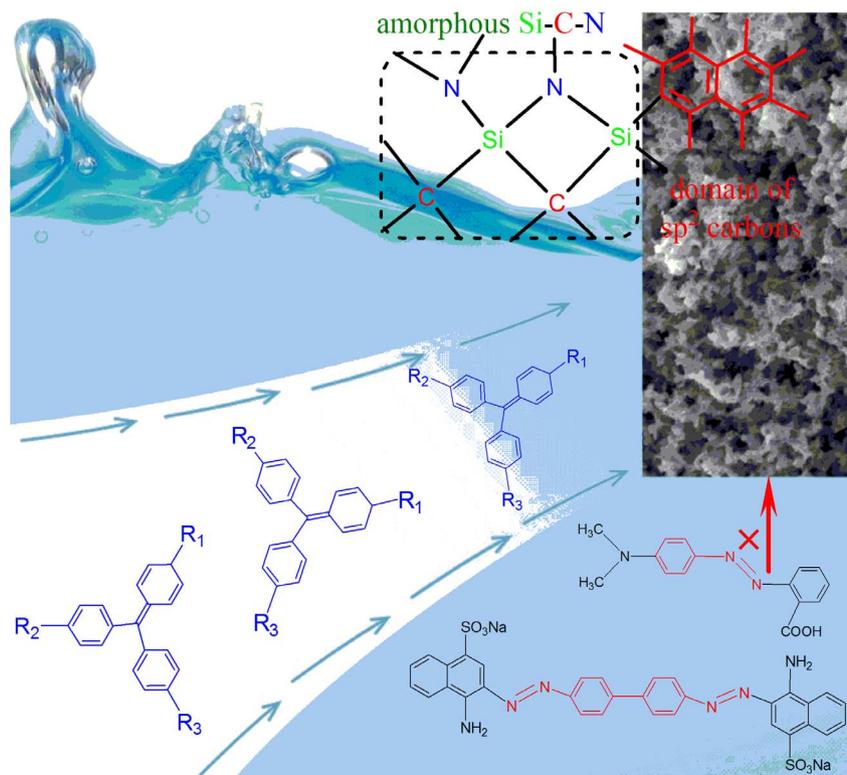

Figure 15 | Schematic illustration of the dyes selective adsorption of Si–C–N porous materials.
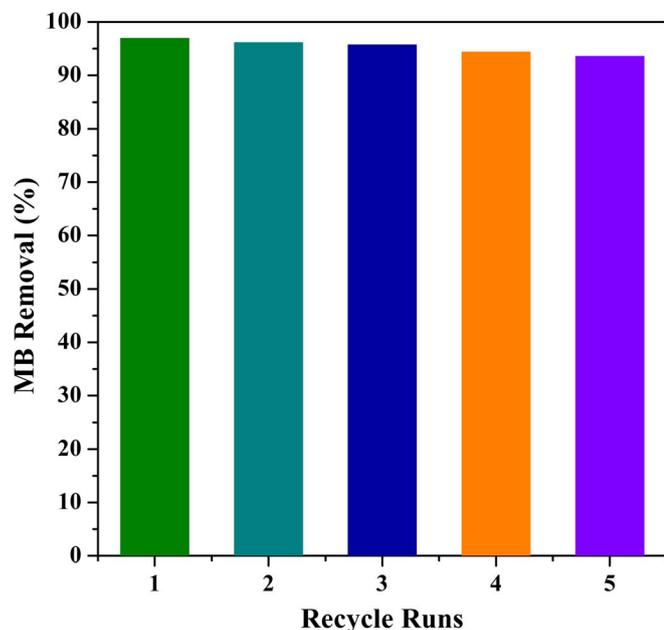
Figure 16 | **Removal percentages of MB in five recycle runs using regenerated C1 (initial concentration: 200 mg·L⁻¹).**

surface of C1. There are no other new peaks observed for C1-MB and C1-AF, thus, indicating that it is a physical adsorption. Figure 18 shows the nitrogen adsorption isotherms, demonstrating that the specific surface area of the porous material dramatically reduces to 3.88 m²·g⁻¹ and 2.19 m²·g⁻¹ for C1-MB and C1-AF, respectively, which indicates that most micropores have been filled with MB and AF molecules after the adsorption. Figure S9 exhibits that the carbon content of C1-MB and C1-AF increase significantly compared to C1 after adsorption, indicating the adsorption of a large number of dye molecules (MB and AF) on C1.

Especially, the MAS Solid-state NMR was employed to give an experimental evidence for the adsorption mechanism. From the ¹³C NMR spectra (Figure 19a), there is an intense peak in the range of 120-150 ppm for C1, which is assigned to sp²-hybridized carbon atoms of Si-C-N materials[70,71]. In addition, the peak at δ 1 ppm is ascribed to sp³-hybridized carbon atoms. For the pure MB, in addition to the broad signal in the range of δ 77–160 ppm assigned to the carbon atoms on the aromatic rings, a small peak at δ 178 ppm may be due to the carbonyl groups caused by air environment. For the C1 after adsorption of MB (C1-MB), the peak of sp²-hybridized carbon atoms at δ 120–150 ppm is significantly higher than that of sp³-hybridized carbon atoms at δ 1 ppm, indicating that numerous MB molecules have been adsorbed to the surface of porous C1. In order to have a clear study on the interaction of sp2-hybridized carbons between C1 and MB, the sp²-hybridization carbon atoms peaks of three samples were fitted using Gaussian peaks as shown in
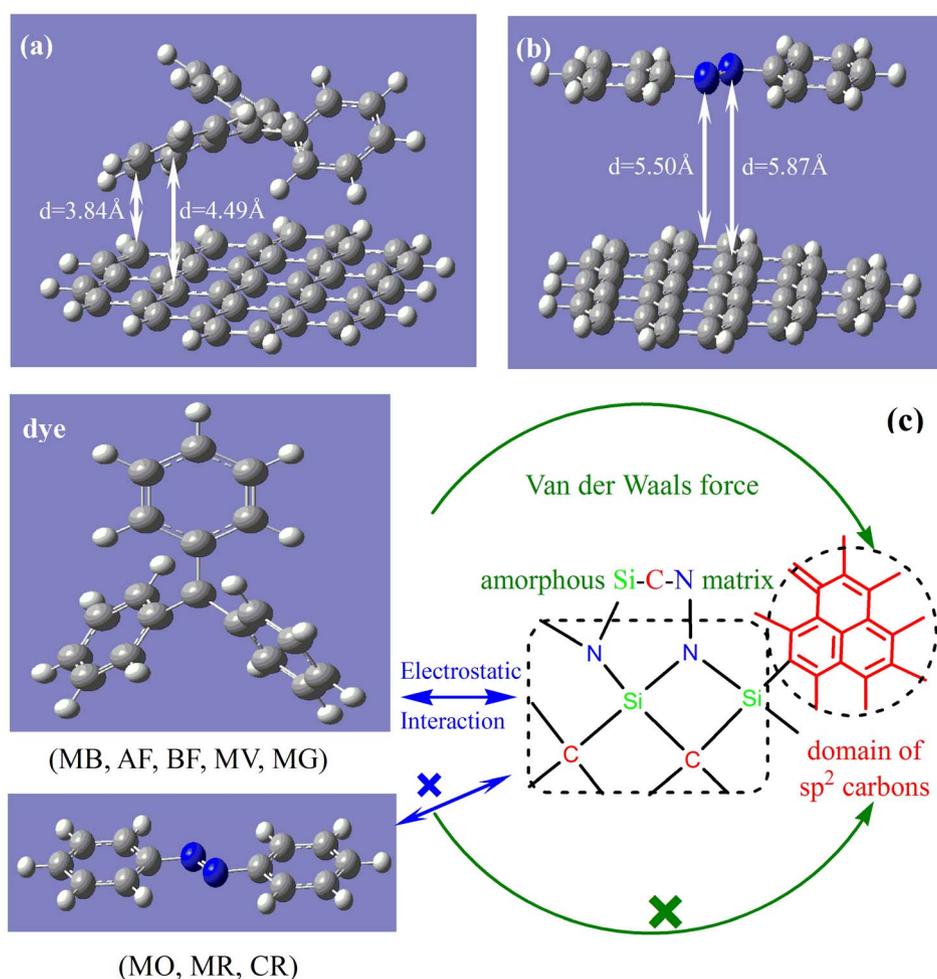

Figure 17 | The suggested selective adsorption mechanism, (a) the interaction between sp² carbon domain and triphenyl structure of MB, (b) the interaction between sp²carbon domain and azo-benzene ring structure of MO calculated according to AM1, (c) suggested selective adsorption mechanism of dyes for porous Si–C–N hybrid material.
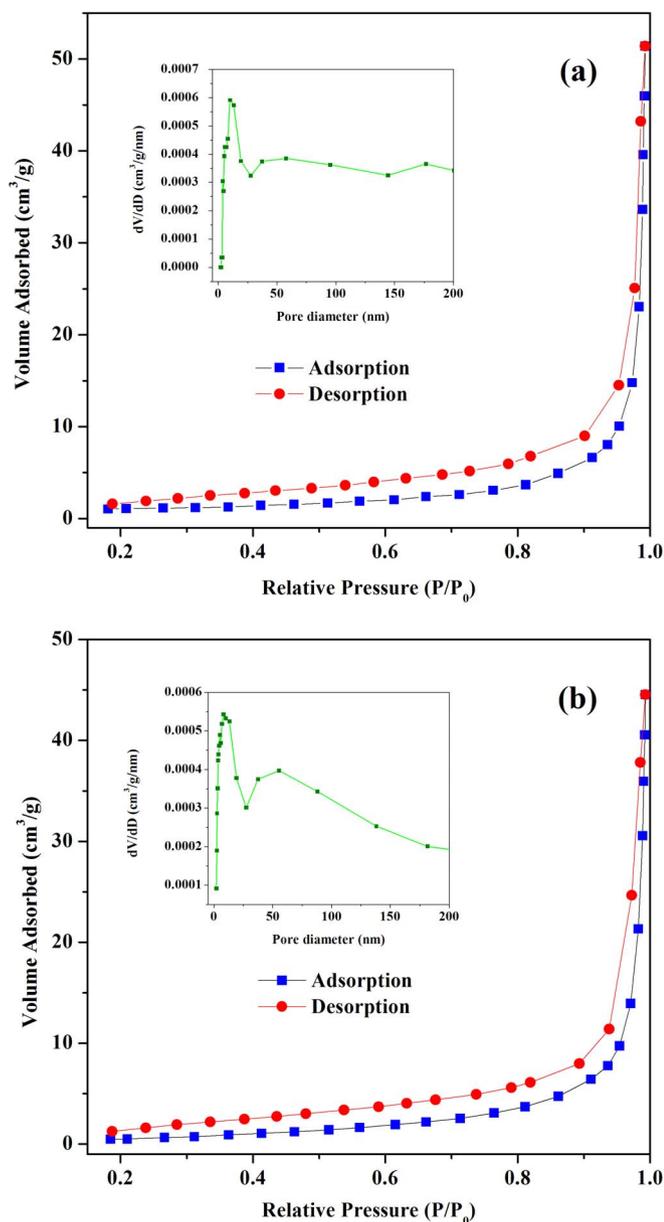
Figure 18 | Nitrogen adsorption–desorption isotherms of (a) C1-MB and (b) C1-AF.

Figure 19 | The MAS Solid-state ^{13}C NMR spectra of MB, C1 and C1-MB (a), and the sp^2-hybridization carbon atoms peaks fitted using Gaussian peaks (b).

Figure 19b. Compared with pure C1 and MB, although no obvious chemical shift in the range of 120–150 ppm changes can be observed for C1-MB, the peak at δ 153.5 ppm derived from the central carbon atoms attached to triphenyl structure of MB was disappeared. It demonstrates that the chemical environmental of the carbon atoms attached to triphenyl structure of MB is changed because of the stack of MB molecules on surface of porous C1. Therefore, the chemical shift those carbons atoms changes towards high-field after adsorption. So the FTIR, XPS and MAS Solid-state NMR measurements mentioned above demonstrate that Van der Waals force between sp^2-hybridized carbon atoms and electrostatic interaction might be the main reason for the highly effective and totally selective adsorption functionality of Si–C–N hybrid materials.

Conclusions

The hierarchically porous Si–C–N hybrid material was prepared by the pyrolysis of polysilazane precursor using PDVB microspheres as sacrificial templates at a lower temperature. The porous Si–C–N hybrid material with high specific surface and interconnected macropores
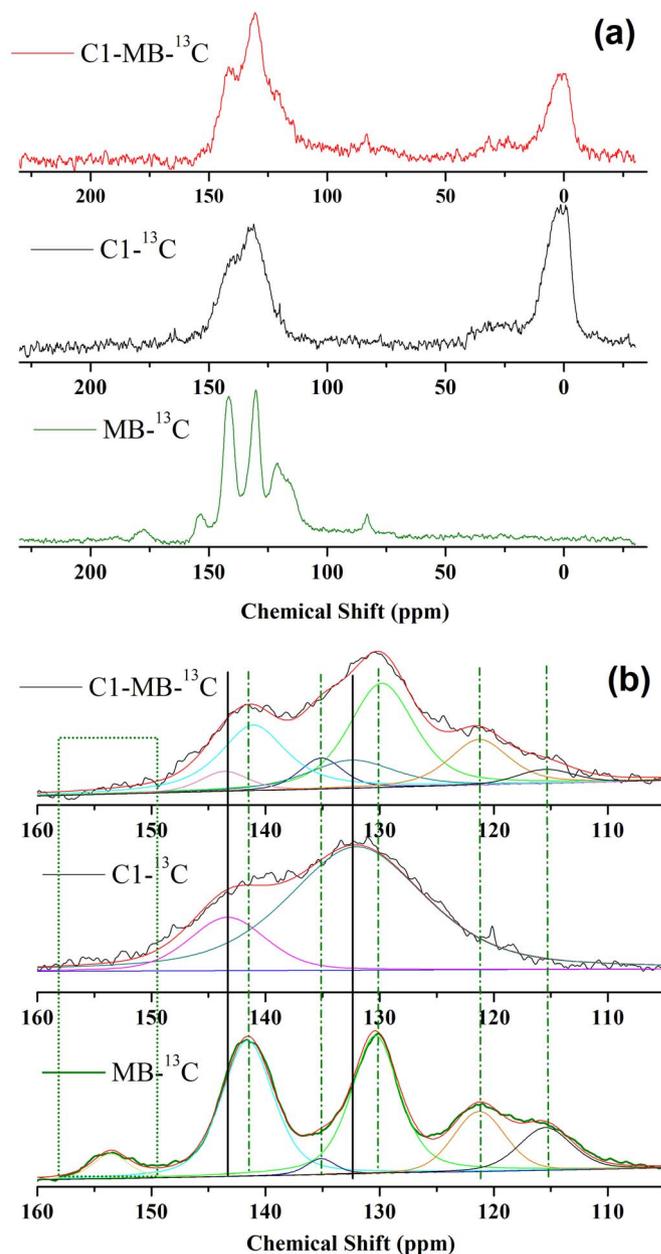
exhibited excellent removal capability for dyes with triphenyl structures due to the Van der Waals force between sp2-hybridized carbon domains or clusters in porous material and triphenyl structure of dyes. Besides, the hybrid material possessed the selective absorption nature toward dyes with triphenyl structure compared to those dyes with azo benzene structures. Langmuir isotherm model showed a better fit with adsorption data than Freundlich isotherm model and the calculated adsorption capacity were 1327.7 mg·g^{-1} for MB and 1084.5 mg·g^{-1} for AF. The adsorption capacity was much higher than that of several other reported adsorbents, such as magnetic chitosan grafted with graphene oxide and organo-bentonite (compared to adsorption for MB), modified cellulose, and carbon nanotube-graphene hybrid aerogel (compared to adsorption for AF). This hierarchically macro/micro hybrid Si–C–N material obtained by a facile and low cost pyrolysis of commercial polymeric precursors exhibited a significant potential in removing organic pollutants from wastewater.

Methods

Materials. The PSZ (The Institute of Chemistry, Chinese Academy of Sciences) was used as-received without further purification. The molar ratio of vinyl groups and silicon hydrogen bonds in main chains was 1 : 4 according to the NMR integral. Nickelocene ($NiCp_2$) was purchased from Strem Chemicals (China). Anhydrous tetrahydrofuran (THF) was freshly distilled under reflux using sodium/benzophenone prior to its use. PDVB microspheres of nominal size 1–1.5 μm were synthesized according to the method reported in the literature[72]. All the dyes (MB, AF, BF, MV, MG, MO, CR and MR) were supplied by Kermel Chemical Reagent Co., Ltd. (Tianjin, China).

Preparation of Hybrid Materials. The PSZ, PDVB microspheres, and $NiCp_2$ were mixed by standard Schlenk techniques because PSZ was relatively sensitive to moisture and oxygen. PSZ (2 g), PDVB (0.6 g), and $NiCp_2$ (0.08 g) were dissolved in anhydrous THF (20 mL). The solution was stirred at room temperature for one day to obtain homogeneous suspension. Hybrid materials with different compositions were prepared by varying the ratio of PSZ, PDVB, and $NiCp_2$ (1 : 0.3 : 0.04, 1 : 0.5 : 0.04, 1 : 1 : 0.04, 1 : 2 : 0.04). Subsequently, the solvent was evaporated under high vacuum using liquid nitrogen trap to make the precursors available as dry powder. Then, the as-prepared dry green powders were transferred into the vertical tube furnace (GSL-1700X, Kejing New Mater. Ltd., China) for cross-linking and pyrolysis under argon atmosphere. Three pyrolysis profiles were developed as follows: first, the precursors were heated to 170°C for cross-linking (holding time: 1 h), pyrolyzed at 600°C for 4 h, and then cooled down to ambient temperature. Second, the precursors were heated from room temperature to 170°C for cross-linking (holding time: 1 h), decomposed at 550°C for 2 h, pyrolyzed at 750°C for 4 h, and then cooled down to ambient temperature. Third, the precursors were heated from room temperature to 170°C for cross-linking (holding time: 1 h), decomposed at 550°C for 2 h, pyrolzed at 1100°C for 4 h, and then cooled down to ambient temperature. The heating and cooling rates for all the experiments were 5 K min^{-1}.

Characterization. The pyrolysis process of precursors was investigated by thermogravimetric (TGA) and differential scanning calorimetry (DSC) analyses by a simultaneous thermoanalyzer STA 449 F3 coupled with a quadrupole mass spectrometer QMS 403 C Aëolos (Netzsch GmbH & Co., Selb, Germany) with a heating rate of 10 K min^{-1} under argon atmosphere (a gas flow of 50 mL min^{-1}) in a temperature range between 40 and 1,300°C. Fourier Transform Infrared Spectroscopy (FTIR) was recorded on a Nicolet ISTO spectrometer (Varian, Palo Alto, California, USA) over a range from 4,000 to 400 cm^{-1}. Raman spectroscopy study was carried out using a Raman Microprobe Instrument (Renishaw, UK) with 514.5 nm Ar+ laser excitation. The MAS Solid-state NMR measurement was performed on a NMR spectrometer (Bruker Anance III-400, Germany). The resonance for ^{13}C was 79.46. All spectra were acquired using magic angle spinning (MAS 54.74) technique with a rotation frequency of 6 kHz for ^{13}C. All samples were measured with a crosspolarization sequence (CP). The recycle delay used was 3 s for ^{13}C and the acquisition time was 42.3 ms for ^{13}C. The adamantine was used as chemical reference for ^{13}C NMR (38.5 ppm from tetra-methylsilane). Powder X-ray diffraction (XRD) measurements were conducted on X′Pert Pro Powder diffractometer (Cu Kα radiation, 40 kV, 40 mA) (PANalytical B.V., Netherlands) using crushed ceramic powders. The X'Celerator scientific RTMS detection unit was used for detection. X-ray photoelectron spectroscopy (XPS) core level spectra were measured using a monochromatic Al K R X-ray source. The analyzer was operated at 23.5 eV pass energy and the analyzed area was 800 μm in diameter. Binding energies were referenced to the adventitious hydrocarbon C1s line at 285.0 eV and the curve fitting of the XPS spectra was performed using the least-squares method. The analysis by scanning electron microscopy (SEM) was performed by a VEGA3 XMH instrument (Tescan Co., Czech Republic). The samples were measured before sputtering a thin layer (1–2 nm) of gold. Pore volume and surface area analysis of the selected porous materials were carried out according to Brunauer–Emmett–Teller (BET) method by nitrogen adsorption–desorption isotherm analysis at −195.8°C (77.35 K, TriStar II 3020, Micromeritics Instrument Co., USA). The powdered samples were degassed at 150°C for 24 h prior to measurement. Specific surface area was calculated using the BET equation. Pore size distributions were derived from the desorption branch of the isotherms using Barrett–Joyner–Halenda (BJH) method.

Dye Adsorption Behavior. The batch mode adsorption was carried out to study the adsorption kinetics and adsorption capacities for dyes, including MB and AF. Dye concentration was determined by measuring at maximum UV absorbance (λ_{max} = 590 nm for MB, λ_{max} = 545 nm for AF). The calibration curves were plotted between absorbance and concentration of dyes to obtain the absorbance-concentration profile based on Beer–Lambert's law (see Table S1–S2 and Figure S10 in Supporting Information). For the kinetic study, solid adsorbent (20 mg) was dispersed in solution (30 mL) with the initial concentration of 200 mg·L^{-1} for MB and AF, respectively. The mixture was continuously allowed to stir in the magnetic stirrer with a speed of 300 rpm at a constant temperature of 25°C. At different time intervals, around 3 mL of suspension was extracted and centrifuged at 4,000 rpm for 5 min for subsequent analysis. For the equilibrium experiment, solid adsorbent (5 mg) was dispersed in dye solution (10 mL) with a certain initial concentration in the range of 300–1200 mg·L^{-1} for MB and 200–900 mg·L^{-1} for AF, respectively. The mixture was allowed to stir continuously for 24 h at ambient temperature until the equilibrium was reached. All the adsorption experiments were conducted twice, and only the

mean values were reported. The maximum deviation for the duplicates was usually less than 5%. The dye concentration in the clear supernatant was determined by a XinMao Ultraviolet–Visible (UV–Vis) spectrophotometer (UV-7504 PC). Besides, the dye solution with high concentration was measured by dilution. The adsorption percentage R (%) and the adsorption capacity Q_e (mg·g^{-1}) were calculated by eqs 8 and 9, respectively.

$$Q_e = (C_0 - C_e) \cdot V / m \qquad (8)$$

$$R(\%) = (C_0 - C_e)/C_0 \cdot 100\% \qquad (9)$$

where C_0 (mg L^{-1}) is the initial concentration, C_e (mg L^{-1}) is the equilibrium concentration after adsorption. V (L) is the solution volume, and m (g) is the mass of the adsorbent. The molecular structures and characteristic properties of representative dyes investigated are shown in Figure 2 and listed in Table S3, respectively.

The Regeneration and Recycling. The recyclability of porous Si–C–N hybrid material was investigated by performing repeated adsorption and regeneration using MB as the model dye. During the adsorption step, porous Si–C–N material (20 mg) was added into MB aqueous solution (40 mL) with an initial concentration of 100 mg·L^{-1}. The suspension was stirred at 300 rpm for 24 h, and then the solid was separated via centrifugation and freeze-dried overnight. The absorbance in the supernatant was determined by UV spectrophotometer. Subsequently, the dried powder was sintered at 400°C for 2 h in vertical tube furnace under nitrogen atmosphere to remove the dye. Notably, there was a loss of about 20% porous material after sintering which was attributed to the mass loss caused by centrifugation. To eliminate the effect of mass loss, a few parallel batches of adsorption/regeneration were conducted at the same time and under the same conditions. After each run, the regenerated porous material from these parallel batches was combined, and the same amount of adsorbent was extracted from this mixture for the next run.

1. Nghiem, Q. D., Asthana, A., Sung, I-K. & Kim, D-P. Fabrication of Porous SiC-Based Ceramic Microchannels via Pyrolysis of Templated Preceramic Polymers. *J. Mater. Res.* **21**, 1543–1549 (2006).
2. Biasetto, L., Francis, A., Palade, P., Principi, G. & Colombo, P. Polymer-Derived Microcellular SiOC Foams with Magnetic Functionality. *J. Mater. Sci.* **43**, 4119–4126 (2008).
3. Sung, I-K., Christian, I. K., Mitchell, M., Kim, D. P. & Kenis, P. J. A. Tailored Macroporous SiCN and SiC Structures for High-Temperature Fuel Reforming. *Adv. Funct. Mater.* **15**, 1336–1342 (2005).
4. Yang, H., Deschatelets, P., Brittain, S. T. & Whitesides, G. M. Fabrication of High Performance Ceramic Microstructures from a Polymeric Precursor Using Soft Lithography. *Adv. Mater.* **13**, 54–57 (2001).
5. Harshe, R., Balan, C. & Riedel, R. Amorphous Si(Al)OC Ceramic from Polysiloxanes: Bulk Ceramic Processing, Crystallization Behavior and Applications. *J. Eur. Ceram. Soc.* **24**, 3471–3482 (2004).
6. Wideman, T. & Sneddon, L. G. Dipentylamine-Modified Polyborazylene: a New, Melt-Spinnable Polymeric Precursor to Boron Nitride Ceramic Fibers. *Chem. Mater.* **8**, 3–5 (1996).
7. Guron, M. M. *et al.* Preceramic Polymer Blends as Precursors for Boron-Carbide/Silicon-Carbide Composite Ceramics and Ceramic Fibers. *Chem. Mater.* **21**, 1708–1715 (2009).
8. Torrey, J. D. *et al.* Composite Polymer Derived Ceramic System for Oxidizing Environments. *J. Mater. Sci.* **41**, 4617–4622 (2006).
9. Melcher, R., Cromme, P., Scheffler, M. & Greil, P. Centrifugal Casting of Thin-Walled Ceramic Tubes from Preceramic Polymers. *J. Am. Ceram. Soc.* **86**, 1211–1213 (2003).
10. Colombo, P. & Bernardo, E. Macro-and Micro-Cellular Porous Ceramics from Preceramic Polymers. *Compos. Sci. Technol.* **63**, 2353–2359 (2003).
11. Nedunchezhian, S., Sujith, R. & Kumar, R. Processing and Characterization of Polymer Precursor Derived Silicon Oxycarbide Ceramic Foams and Compacts. *J. Adv. Ceram.* **2**, 318–324 (2013).
12. Prasad, R. M. *et al.* Thermal Decomposition of Carbon-Rich Polymer-Derived Silicon Carbonitrides Leading to Ceramics with High Specific Surface Area and Tunable Micro- and Mesoporosity. *J. Eur. Ceram. Soc.* **32**, 477–484 (2012).
13. Nghiem, Q. D. & Kim, D. P. Direct Preparation of High Surface Area Mesoporous SiC-Based Ceramic by Pyrolysis of a Self-Assembled Polycarbosilane-Block-Polystyrene Diblock Copolymer. *Chem. Mater.* **20**, 3735–3739 (2008).
14. Kleebe, H. J., Störmer, H., Trassl, S. & Ziegler, G. Thermal Stability of SiCN Ceramics Studied by Spectroscopy and Electron Microscopy. *Appl. Organomet. Chem.* **15**, 858–866 (2001).
15. Bharadwaj, L., Fan, Y., Zhang, L., Jiang, D. & An, L. Oxidation Behavior of a Fully Dense Polymer-Derived Amorphous Silicon Carbonitride Ceramic. *J. Am. Ceram. Soc.* **87**, 483–486 (2004).
16. Shah, S. R. & Raj, R. Mechanical Properties of a Fully Dense Polymer Derived Ceramic Made by a Novel Pressure Casting Process. *Acta Mater.* **50**, 4093–4103 (2002).

17. Francis, A., Ionescu, E., Fasel, C. & Riedel, R. Crystallization Behavior and Controlling Mechanism of Iron-Containing Si-C-N Ceramics. *Inorg. Chem.* **48**, 10078–10083 (2009).
18. Wilhelm, M., Soltmann, C., Koch, D. & Grathwohl, G. Ceramers-Functional Materials for Adsorption Techniques. *J. Eur. Ceram. Soc.* **25**, 271–276 (2005).
19. Adam, M., Wilhelm, M. & Grathwohl, G. Polysiloxane Derived Hybrid Ceramics with Nanodispersed Pt. *Micropor. Mesopor. Mater.* **151**, 195–200 (2012).
20. Wilhelm, M., Adam, M., Bäumer, M. & Grathwohl, G. Synthesis and Properties of Porous Hybrid Materials Containing Metallic Nanoparticles. *Adv. Eng. Mater.* **10**, 241–245 (2008).
21. Sonstrom, P. *et al.* Colloidal Nanoparticles Embedded in Ceramers: toward Structurally Designed Catalysts. *J. Phys. Chem. C* **114**, 14224–14232 (2010).
22. Adam, M., Kocanis, S., Fey, T., Wilhelm, M. & Grathwohl, G. Hierarchically Ordered Foams Derived from Polysiloxanes with Catalytically Active Coatings. *J. Eur. Ceram. Soc.* **34**, 1715–725 (2014).
23. Iqbal, M. J. & Ashiq, M. N. Adsorption of Dyes from Aqueous Solutions on Activated Charcoal. *J. Hazard. Mater.* **139**, 57–66 (2007).
24. Garg, V. K., Amita, M., Kumar, R. & Gupta, R. Basic Dye (Methylene Blue) Removal from Simulated Wastewater by Adsorption Using Indian Rosewood Sawdust: a Ttimber Industry Waste. *Dyes. Pigments.* **63**, 243–250 (2004).
25. Haque, E., Jun, J. W. & Jhung, S. H. Adsorptive Removal of Methyl Orange and Methylene Blue from Aqueous Solution with a Metal-Organic Framework Material, Iron Terephthalate (MOF-235). *J. Hazard. Mater.* **185**, 507–511 (2011).
26. Robinson, T., Chandran, B. & Nigam, P. Removal of Dyes from a Synthetic Textile Dye Effluent by Biosorption on Apple Pomace and Wheat Straw. *Water Res.* **36**, 2824–2830 (2002).
27. El-Gohary, F. & Tawfik, A. Decolorization and COD Reduction of Disperse and Reactive Dyes Wastewater Using Chemical-Coagulation Followed by Sequential Batch Reactor (SBR) Process. *Desalination* **249**, 1159–1164 (2009).
28. Lachheb, H. *et al.* Photocatalytic Degradation of Various Types of Dyes (Alizarin S, Crocein Orange G, Methyl Red, Congo Red, Methylene Blue) in Water by UV-irradiated Titania. *Appl. Catal. B: Environ.* **39**, 75–90 (2002).
29. He, C. & Hu, X. Anionic Dye Adsorption on Chemically Modified Ordered Mesoporous Carbons. *Ind. Eng. Chem. Res.* **50**, 14070–14083 (2011).
30. Hameed, B. H. A Novel Sorbent for the Removal of Basic Dye from Aqueous Solution. *J. Hazard. Mater.* **166**, 233–238 (2009).
31. Ho, Y. S., Chiu, W. T. & Wang, C. C. Regression Analysis for the Sorption Isotherms of Basic dyes on Sugarcane Dust. *Bioresour. Technol.* **96**, 1285–1291 (2005).
32. Iram, M., Guo, C., Guan, Y., Ishfaq, A. & Liu, H. Adsorption and Magnetic Removal of Neutral Red Dye from Aqueous Solution Using Fe_3O_4 Hollow Nanospheres. *J. Hazard. Mater.* **181**, 1039–1050 (2010).
33. Mohammadi, N., Khani, H., Gupta, V. K., Amereh, E. & Agarwal, S. Adsorption Process of Methyl Orange Dye onto Mesoporous Carbon Material-Kinetic and Thermodynamic Studies. *J. Colloid Interface Sci.* **362**, 457–462 (2011).
34. Xu, J., Wang, L. & Zhu, Y. Decontamination of Bisphenol A from Aqueous Solution by Graphene Adsorption. *Langmuir* **28**, 8418–8425 (2012).
35. Ziegler, G. *et al.* Synthesis, Microstructure and Properties of SiCN Ceramics Prepared from Tailored Polymers. *Mater. Chem. Phys.* **61**, 55–63 (1999).
36. SeifollahiBazarjani, M. *et al.* Nanoporous Silicon Oxycarbonitride Ceramics Derived from Polysilazanes in Situ Modified with Nickel Nanoparticles. *Chem. Mater.* **23**, 4112–4123 (2011).
37. Hurwitz, F. I., Heimann, P., Farmer, S. C. & Hembree Jr, D. M. Characterization of the Pyrolytic Conversion of Polysilsesquioxanes to Siliconoxycarbides. *J. Mater. Sci.* **28**, 6622–6630 (1993).
38. Mera, G., Riedel, R., Poli, F. & Müller, K. Carbon-Rich SiCN Ceramics Derived from Phenyl-Containing Poly(silylcarbodiimides). *J. Eur. Ceram. Soc.* **29**, 2873–2883 (2009).
39. Colombo, P., Mera, G., Riedel, R. & Sorarù, G. D. Polymer-Derived Ceramics: 40 Years of Research and Innovation in Advanced Ceramics. *J. Am. Ceram. Soc.* **93**, 1805–1837 (2010).
40. Qi, X. *et al.* Magnetic Properties and Large-Scale Synthesis of Novel Carbon Nanocomposites via Benzene Decomposition over Ni Nanoparticles. *J. Phys. Chem. C.* **113**, 2267–2272 (2009).
41. Karlin, S. & Colomban, P. Raman Study of the Chemical and Thermal Degradation of As-Received and Sol-Gel Embedded Nicalon and Hi-Nicalon SiC Fibres Used in Ceramic Matrix Composites. *J. Raman Spectrosc.* **28**, 219–228 (1997).
42. Ferrari, A. C. & Robertson, J. Resonant Raman Spectroscopy of Disordered, Amorphous, and Diamondlike Carbon. *Phys. Rev. B.* **64**, 075414 (2001).
43. Waldrop, J. R., Grant, R. W., Wang, Y. C. & Davis, R. F. Metal Schottky barrier contacts to alpha 6H-SiC. *J. Appl. Phys.* **72**, 4757 (1992).
44. Swain, B. P. The Analysis of Carbon Bonding Environment in HWCVD Deposited a-SiC:H Films by XPS and Raman Spectroscopy. *Surf. Coat. Tech.* **201**, 1589–1593 (2006).
45. Saha, S. K., Howell, R. S. & Hatalis, M. K. Silicidation Reactions with Co-Ni Bilayers for Low Thermal Budget Microelectronic Applications. *Thin Solid Films.* **347**, 278–283 (1999).
46. Huntley, D. R. The Mechanism of the Desulfurization of Benzenethiol by Nickel (110). *J. Chem. Phys.* **96**, 4550–4558 (1992).
47. Rufael, T. S., Huntley, D. R., Mullins, D. R. & Gland, J. L. Adsorption and Reaction of Dimethyl Disulfide on the Ni (111) Surface. *J. Phys. Chem. C.* **102**, 3431–3440 (1998).
48. Ingo, G. M., Zacchetti, N., Della Sala, D. & Coluzza, C. XPS Investigation on Amorphous Silion Nitride (a-SiNx) Chemical Structure. *Surf. Interface Anal.* **12**, 323–324 (1988).
49. Schmidt, H., Koch, D., Grathwohl, G. & Colombo, P. Micro-/Macroporous Ceramics from Preceramic Precursors. *J. Am. Ceram. Soc.* **84**, 2252–2255 (2001).
50. Kroke, E. *et al.* Silazane Derived Ceramics and Related Materials. *Mat. Sci. Eng. R.* **26**, 97–199 (2000).
51. Wan, J., Gasch, M. J. & Mukherjee, A. K. In Situ Densification Behavior in the Pyrolysis Consolidation of Amorphous Si-N-C Bulk Ceramics from Polymer Precursors. *J. Am. Ceram. Soc.* **84**, 2165–2169 (2001).
52. Ghaedi, M., Hassanzadeh, A. & Kokhdan, S. N. Multiwalled Carbon Nanotubes as Adsorbents for the Kinetic and Equilibrium Study of the Removal of Alizarin Red S and Morin. *J. Chem. Eng. Data* **56**, 2511–2520 (2011).
53. Ho, Y. S. & McKay, G. Sorption of Dye from Aqueous Solution by Peat. *Chem. Eng. J.* **70**, 115–124 (1998).
54. Ayad, M. M. & El-Nasr, A. A. Adsorption of Cationic Dye (Methylene Blue) from Water Using Polyaniline Nanotubes Base. *J. Phys. Chem. C.* **114**, 14377–14383 (2010).
55. Weber, W. J. & Morris, J. C. Kinetics of Adsorption on Carbon from Solution. *J. Sanit. Eng. Div. Am. Soc. Civ. Eng.* **89**, 31–60 (1963).
56. Ai, L., Zhang, C. & Meng, L. Adsorption of Methyl Orange from Aqueous Solution on Hydrothermal Synthesized Mg-Al Layered Double Hydroxide. *J. Chem. Eng. Data* **56**, 4217–225 (2011).
57. Ghorai, S. *et al.* Enhanced Removal of Methylene Blue and Methyl Violet Dyes from Aqueous Solution Using a Nanocomposite of Hydrolyzed Polyacrylamide Grafted Xanthan Gum and Incorporated Nanosilica. *ACS Appl. Mater. Interfaces* **6**, 4766–4777 (2014).
58. Langmuir, I. The Adsopption of Gases on Plane Surfaces of Glass, Mica and Platinum. *J. Am. Chem. Soc.* **40**, 1361–1403 (1918).
59. Fan, L. *et al.* Fabrication of Novel Magnetic Chitosan Grafted with Graphene Oxide to Enhance Adsorption Properties for Methyl Blue. *J. Hazard. Mater.* **215**, 272–279 (2012).
60. Shao, Y. *et al.* Application of Mn/MCM-41 as an Adsorbent to Remove Methyl Blue from Aqueous Solution. *J. Colloid Interface Sci.* **429**, 25–33 (2014).
61. Hao, X. *et al.* Magnetic Field Assisted Adsorption of Methyl Blue onto Organo-Bentonite. *Appl. Clay Sci.* **55**, 177–180 (2012).
62. Zhang, F. *et al.* Selective and Effective Adsorption of Methyl Blue by Barium Phosphate Nano-Flake. *J. Colloid Interface Sci.* **386**, 277–284 (2012).
63. Fan, L. *et al.* Synthesis and Characterization of Magnetic β-Cyclodextrin-Chitosan Nanoparticles as Nano-Adsorbents for Removal of Methyl Blue. *Int. J. Biol. Macromol.* **50**, 444–450 (2012).
64. Zhou, Y., Hu, X., Zhang, M., Zhuo, X. & Niu, J. Preparation and Characterization of Modified Cellulose for Adsorption of Cd(II), Hg(II), and Acid Fuchsin from Aqueous Solutions. *Ind. Eng. Chem. Res.* **52**, 876–884 (2013).
65. Dutta, S. & Basu, J. K. Fixed-Bed Column Study for the Adsorptive Removal of Acid Fuchsin Using Carbon–Alumina Composite Pellet. *Int. J. Environ. Sci. Tech.* **11**, 87–96 (2014).
66. Sui, Z., Meng, Q., Zhang, X., Ma, R. & Cao, B. Green Synthesis of Carbon Nanotube-Graphene Hybrid Aerogels and Their use as Versatile Agents for Water Purification. *J. Mater. Chem.* **22**, 8767–8771 (2012).
67. Freundlich, H. *Colloid and Capillary Chemistry; Methuen: London, 1926.*
68. Ma, J. *et al.* Enhanced Adsorptive Removal of Methyl Orange and Methylene Blue from Aqueous Solution by Alkali-Activated Multiwalled Carbon Nanotubes. *ACS Appl. Mater. Interfaces* **4**, 5749–5760 (2012).
69. Liu, Y. *et al.* An ONIOM Study of H2O Interacting with the C-Terminated Surface of Silicon Carbide. *Chem. Phys. Lett.* **501**, 87–92 (2010).
70. Gerardin, C., Taulelle, F. & Livage, J. Pyrolysis of a Polyvinylsilazane,Polymeric Precursor for Silicon Carbonitride: Structural Investigation by 1H, 13C, 29Si, 15N and 14N Nuclear Magnetic Resonance. *J. Chim. Phys.* **89**, 461–467 (1992).
71. Seitz, J., Bill, J., Egger, N. & Aldinger, F. Structural Investigations of Si/C/N-Ceramics from Polysilazane Precursors by Nuclear Magnetic Resonance. *J. Eur. Ceram. Soc.* **16**, 885–91 (1996).
72. Bai, F., Yang, X. & Huang, W. Synthesis of Narrow or Monodisperse Poly (divinylbenzene) Microspheres by Distillation-Precipitation Polymerization. *Macromolecules* **37**, 9746–9752 (2004).

Acknowledgments

Author contributions

J.K. designed the experiments, analysed the data and led the project. L.M. and X.Z. executed the experiments and analysed the data. Y.T. analysed the data. K.S. performed the

Additional information